

1 A FIELD VALIDATED SURROGATE CROP MODEL FOR
2 PREDICTING ROOTZONE MOISTURE AND SALT CONTENT IN
3 REGIONS WITH SHALLOW GROUNDWATER

4 Zhongyi Liu¹, Zailin Huo^{1*}, Chaozi Wang¹, Limin Zhang², Xianghao Wang¹,
5 Guanhua Huang¹, Xu Xu¹, Tammo S. Steenhuis^{3*}

6
7 1. Center for Agricultural Water Research in China, China Agricultural University, Beijing,
8 100083, PR China

9 2. School of Water Resources and Environment, China University of Geosciences, Beijing,
10 100083, PR, China

11 3. Department of Biological and Environmental Engineering, Cornell University, Ithaca, NY,
12 USA.

13
14 Correspondence to: Zailin Huo (huozl@cau.edu.cn)

15 Tammo S. Steenhuis (tss1@cornell.edu)

22 **Abstract**

23 Optimum [management](#) of irrigated crops in regions with shallow saline groundwater
24 requires a careful balance between application of irrigation water and upward
25 movement of salinity from the groundwater. Few field validated surrogate models are
26 available to aid in the management of irrigation water under shallow groundwater
27 conditions. The objective of this research is to develop a model that can aid in the
28 management using a minimum of input data that is field validated. In this paper a
29 2-year field experiment was carried out in the Hetao irrigation district in Inner
30 Mongolia, China and a physically based integrated surrogate model for arid irrigated
31 areas with shallow groundwater was developed and validated with the collected field
32 data. The integrated model that links crop growth with available water and salinity in
33 the vadose zone is called Evaluation of the Performance of Irrigated Crops and Soils
34 (EPICS). EPICS recognizes that field capacity is reached when the matric potential is
35 equal to the height above the groundwater table and thus not by a limiting hydraulic
36 conductivity. In the field experiment, soil moisture contents and soil salt conductivity
37 at 5 depths in the top 100 cm, groundwater depth, crop height, and leaf area index
38 were measured in 2017 and 2018. The field results were used for calibration and
39 validation of EPICS. Simulated and observed data fitted generally well during both
40 calibration and validation. The EPICS model that can predict crop growth, soil water,
41 groundwater depth and soil salinity can aid in optimizing water management in
42 irrigation districts with shallow aquifers.

43 **Key words:** Surrogate hydrological model, irrigated crops, shallow aquifer

Nomenclature			
ET ₀	Reference evapotranspiration (mm)	p	Fraction of readily available soil water relative to the total available soil water
ET _P	Potential evapotranspiration (mm)	S	Salt stress coefficient ()
E _p	Potential evaporation (mm)	B	Crop specific parameter (%)
T _p	Potential transpiration (mm)	k _y	Factor that affects crop yield
E _a	Actual evaporation (mm)	E _{Ce}	Electrical conductivity of the soil saturation extract (mS cm ⁻¹)
T _a	Actual transpiration (mm)	EC _{ethreshold}	Threshold of the electrical conductivity of the soil saturation extract when the crop yield becomes affected by salt (mS cm ⁻¹)
K _c	Crop coefficient()	EC _{1:5}	Electrical conductivity of the soil extract that soil samples mixed with distilled water in a proportion of 1:5 (mS cm ⁻¹)
τ	Development stage of the leaf canopy()	θ _s	Soil moisture content at saturation (cm ⁻³ cm ⁻³)
r _τ	Root function for transpiration ()	φ _b	Bubbling pressure (cm)
r _E	Root function for transpiration ()	φ _m	Matric potential (cm)
j	Number of soil layer()	λ	Pore size distribution index
LAI	Leaf area index()	h	Groundwater depth (cm)
T _{mean}	Mean daily temperature (°C)	z	Depth of the point below the soil surface (cm)
T _{mx}	Maximum daily temperature (°C)	W _{fc} (h)	Total water content at field capacity of the soil profile over a prescribed depth (cm)
T _{mn}	Minimum daily temperature (°C)	L(j)	Height of layer j (cm)
LAI _{mx}	Maximum leaf area index	μ	Drainable porosity
RD _{mx}	Maximum root depth (cm)	P	Precipitation (mm)
K _b	Dimensionless canopy extinction coefficient	I	Irrigation (mm)
PHU	Total potential heat units required for crop maturation (°C)	n	Number of soil layers
Z _{1j}	Depth of the upper boundaries of soil layer j (cm)	R _{gw}	Percolation to groundwater (mm)
Z _{2j}	Depth of the lower boundaries of the soil layer for r _E (j,t); root depth or the lower boundaries of the soil layer for r _τ (j,t) (cm)	R _w (j-1,t)	Percolation rate to layer j from layer j-1 at day t (mm)
δ	Water use distribution parameter	C(j,t)	Salt concentration of layer j at day t (g L ⁻¹)
k _E	Water stress coefficient for evaporation	C _I	Salt concentration of irrigation water (g L ⁻¹)
k _τ	Water stress coefficient for transpiration	C _{gw}	Salt concentration of groundwater (g L ⁻¹)
θ	Soil moisture content (cm ⁻³ cm ⁻³)	U _{gw}	Actual upward flux of groundwater (mm)
θ _{fc}	Soil moisture content at field capacity (cm ⁻³ cm ⁻³)	U _{gw,max}	Maximum upward flux of groundwater (mm)
θ _r	Soil moisture content at wilting point (cm ⁻³ cm ⁻³)	a	Constant used for calculation of U _{gw,max} ()
f _{shape}	Shape factor of k _τ curve ()	b	Constant used for calculation of U _{gw,max} ()

45 **1. Introduction**

46 Irrigation water is a scarce resource, especially in arid and semi-arid areas of the
47 world. Irrigation improves quality and quantity of food production; however, excess
48 irrigation and salinization remain one of the key challenges. Almost 20% of the
49 irrigated land in the world is affected by salinization and this percentage is still on the
50 rise (Li et al., 2014). Soil salinization and water shortages, especially associated with
51 surface irrigated agriculture in arid to semi-arid areas, is a threat to the well-being of
52 local communities in these areas (Dehaan and Taylor, 2002; Rengasamy, 2006).

53 In arid and semi-arid [areas where people divert surface water for flood irrigation](#)
54 and [have poor](#) drainage infrastructures, the groundwater table is close to the surface
55 because more water has been applied than crop evapotranspiration. Capillary rise of
56 the shallow groundwater can be used to supplement irrigation and thereby, in closed
57 basins, can possibly save water for irrigating additional areas downstream (Gao et al.,
58 2015; Yeh and Famiglietti, 2009; Luo and Sophocleous, 2010.). However, at the same
59 time, capillary upward moving water carries salt from the groundwater increasing the
60 salt in the upper layers of the soil leading to soil degradation and possibly decreasing
61 yields and change of crop patterns to more salt tolerant crops (Guo et al., 2018;
62 Huang et al., 2018). The leaching of salts with irrigation water is necessary and useful
63 for irrigated agriculture (Letey et al., 2011). In north China, the fields are commonly
64 irrigated in the autumn before soil freezing to leach salts and provide water for first
65 growth after [seeding](#) in the following year (Feng et al., 2005).

66 Tradeoffs between irrigation practices and soil salinity were studied by a lot of

67 researchers (Hanson et al., 2008; Pereira et al., 2002, 2009; Minhas et al., 2020).
68 Minhas et al. (2020) give a brief review of crop evapotranspiration and water
69 management issues when coping with salinity in irrigated agriculture. Phogat et al.
70 (2020) assessed the effects of long-term irrigation on salt build-up in the soil under
71 unheated greenhouse conditions by the UNSA-TCHEM and HYDRUS-1D (Phogat et
72 al., 2020).

73 Therefore, understanding the interaction of improved crop yield, soil salinization
74 and decreased surface irrigation is important to the sustainability of the surface
75 irrigation water systems in arid and semi-arid areas. This will require experimentation
76 under realistic farmers' field conditions, as well as modeling to extend the findings
77 beyond the plot scale.

78 Field scale models for water, solute transport and crop growth are widely
79 available. Crop growth models use either empirical functions or model the underlying
80 physiological processes (Liu, 2009). Models widely used for simulating crop growth
81 are EPIC (Williams et al., 1989), DSSAT (Uehara, 1989), WOFOST (Diepen et al.,
82 1989) and AquaCrop (Hsiao et al., 2009; Raes et al., 2009; Steduto et al., 2009).
83 Models focused on water and solute movement in the vadose zone using some form
84 of Richards' equation are HYDRUS (Šimůnek et al., 1998) and SWAP (Dam et al.,
85 1997). Models that integrate crop growth and water-solute movement processes are
86 SWAP-WOFOST (Hu et al., 2019), SWAP-EPIC (Xu et al., 2015; Xu et al., 2016),
87 HYDRUS-EPIC ((Wang et al., 2015), and HYDRUS-DSSAT (Shelia et al., 2018).
88 These integrated models require input data that are usually not available when

89 applied over extended areas (Liu et al., 2009; Xu et al., 2016; Hu et al., 2019). The
90 EPIC crop growth model is often preferred in integrated crop growth hydrology
91 models because it requires relatively few input data and is accurate (Wang et al.,
92 2014; Xu et al., 2013; Chen et al., 2019).

93 There is a tendency with the advancement of computer technology to include
94 more physical processes in these models (Asher et al., 2015; Doherty and Simmons,
95 2013; Leube et al., 2012). Detailed [spatial](#) input of soil hydrological properties and
96 crop growth are required to take advantage of the model complexity (Flint et al., 2002;
97 Rosa et al., 2012). This greater model complexity, both in space and time, requires
98 longer model run times, especially for the time-dependent models (Leube et al., 2012).
99 These models are useful for research purposes but for actual field applications, the
100 required input data are not available and expensive to obtain. In such cases, simpler
101 surrogate models are a good alternative (Blanning, 1975; Willcox and Peraire, 2002;
102 Regis and Shoemaker, 2005). Surrogate models run faster and are as accurate as
103 the complex models for a specific problem (shallow groundwater here) but not as
104 versatile as the more complex models that can be applied over a wide range of
105 conditions (Asher et al., 2015).

106 Simple surrogate models are abundant in China for areas where the groundwater
107 is deeper than approximately 10 m (Kendy et al., 2003; Chen et al., 2010; Ma et al.,
108 2013; Li et al., 2017; Wu et al., 2016), but are limited and relatively scarce for areas
109 where the groundwater is near the surface in the arid to semi-arid areas (Xue et al.,
110 2018; Gao et al., 2017; Liu et al., 2019). In these areas with shallow aquifer, the

111 upward groundwater flux from groundwater is an important factor in meeting the
112 evapotranspiration demand of the crop (Babajimopoulos et al., 2007; Yeh and
113 Famiglietti, 2009). The advantage of applying surrogate models in areas with shallow
114 aquifer is that they can simulate the hydrological process with fewer parameters using
115 with simpler and computationally less demanding mathematical relationships than the
116 traditional finite element or difference models (Wu et al., 2016; Razavi et al., 2012).

117 The change in matric potential is often ignored in these surrogate models for
118 soils with a deep groundwater table. However, for areas with shallow aquifers (i.e.,
119 less than approximately 3 m), the matric potential cannot be ignored. The flow of
120 water is upward when the absolute value of matric potential is greater than the
121 groundwater depth or downward when it is less than the groundwater depth (Gardner,
122 1958; Gardner et al., 1970a; b; Steenhuis et al., 1988). The field capacity in these
123 soils is reached when the hydraulic gradient is constant (i.e., the constant value of
124 sum of matric potential and gravity potential). In this case, the soil water is in
125 equilibrium and no flow occurs.

126 Xue et al. (2018) and Gao et al. (2017), developed models for the shallow
127 groundwater, but used field capacities and drainable porosities that were calibrated
128 and independent of the depth of the groundwater. This is inexact when the
129 groundwater is close to the surface. Liu et al. (2019), used for simulating shallow
130 groundwater the same type of model as described in this paper but calibrated crop
131 evaporation and did not simulate the salt concentrations in the soil. This made their
132 model less useful for practical application.

133 Because of the shortcomings in the above complex models, we avoided the use
134 of a constant drainable porosity and considered the crop growth and thus improved
135 the surrogate model in our last study (Liu et al., 2019). The objective of this research
136 was to develop a field validated surrogate model that could be used to simulate the
137 water and salt movement and crop growth in irrigated areas with shallow groundwater
138 and salinized soil with a minimum of input parameters. To validate the surrogate
139 model, we performed a 2-year field experiment in the Hetao irrigation district that
140 investigated the change in soil salinity, moisture content, groundwater depth and
141 maize and sunflower growth during the growing season.

142 In the following section we present first the theoretical background of the
143 surrogate model. The model consists of crop growth module and a vadose zone
144 module. This is followed by detailed description of the two-year field experiments
145 [started](#) in 2017 in the Hetao irrigation district where maize and sunflower were
146 irrigated by flooding the field. The experimental results consisting of climate data,
147 irrigation application, crop growth parameters, moisture and salt content and
148 groundwater depth are used to calibrate and validate the model.

149 **2. Model description**

150 2.1 Introduction of the model

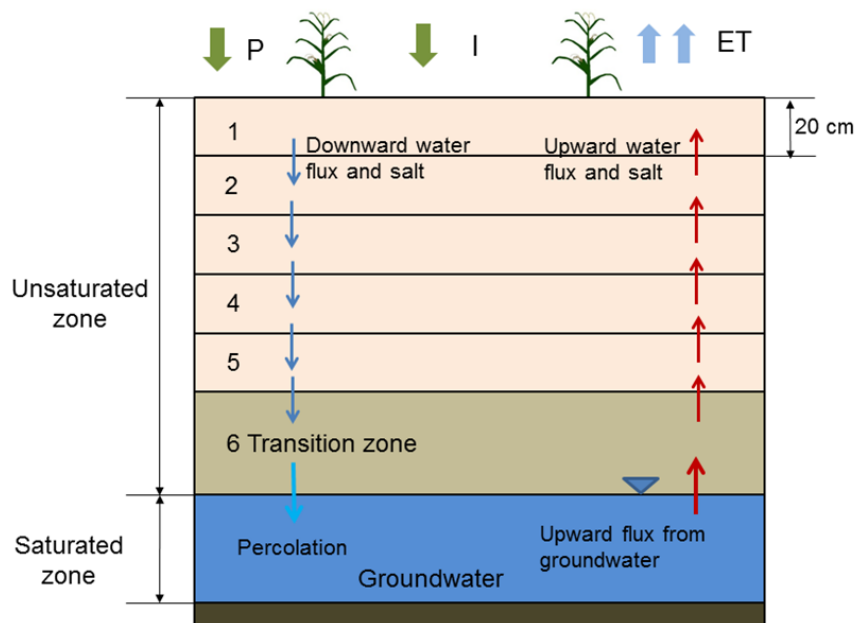
151 In a recent study, we presented a surrogate model for the vadose zone with shallow
152 groundwater using the novel concept that the moisture content at field capacity is a
153 unique function of the groundwater depth after irrigation or precipitation that wets up
154 the entire soil profile. The model, called the Shallow Vadose Groundwater model,

155 applies directly to surface irrigated districts where the groundwater is within 3.3 m
 156 from the soil surface (Liu et al. 2019). The model was a proof of concept with
 157 calibrated values for evapotranspiration and soil salinity which was not simulated.

158 To make the Shallow Vadose Groundwater model more physically realistic, we
 159 added a crop growth model and included the effect of salinity and moisture content on
 160 evaporation and transpiration directly in this study. The new model that combines
 161 parts of the EPIC (Erosion Productivity Impact Calculator, Williams et al., 1989) with
 162 Shallow Vadose Groundwater model is called the *Evaluation of the Performance of*
 163 *Irrigated Crops and Soils* (EPICS).

164 2.2 Structure of the EPICS model

165 In the EPICS model, the soil profile is divided into five layers of 20 cm (from the soil
 166 surface down) and a sixth layer that stretches from the 100 cm depth to the water
 167 table below (Fig. 1).

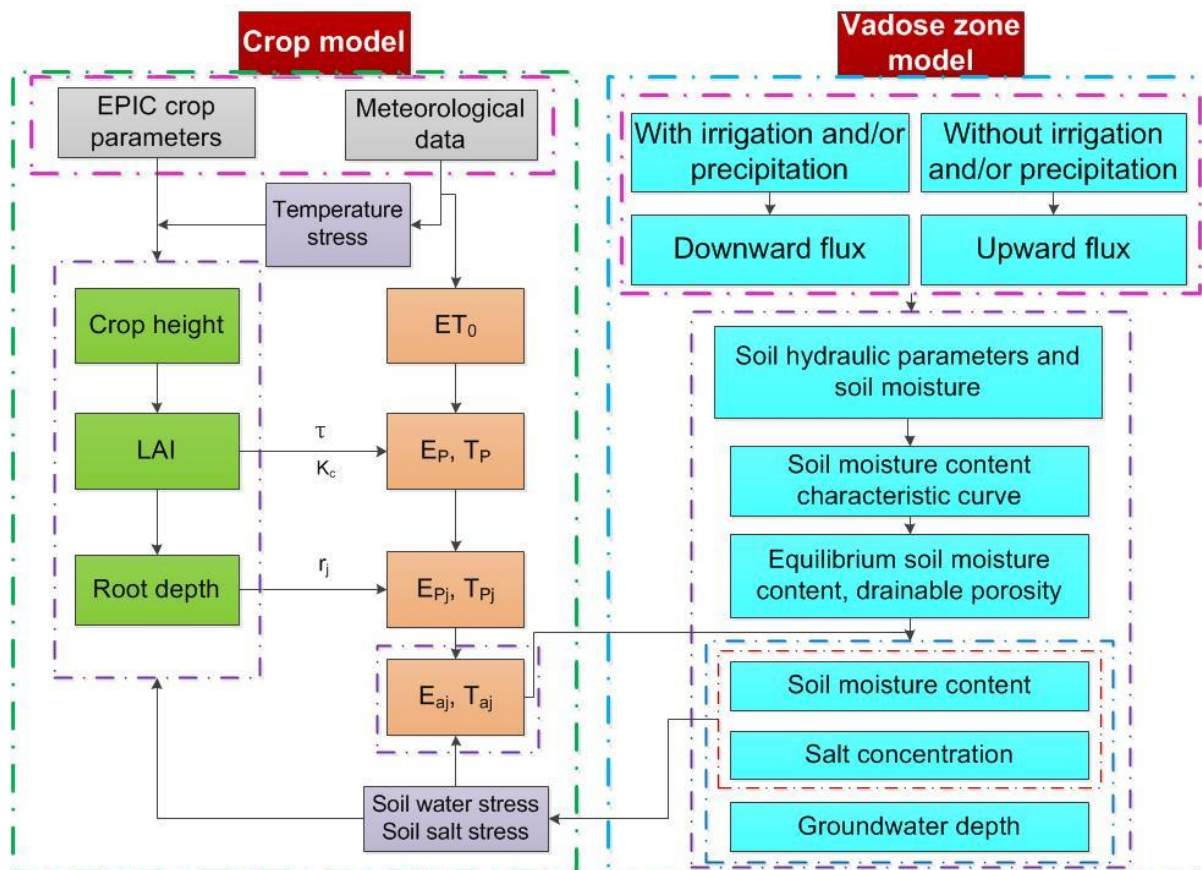


168

169 Fig 1. Schematic diagram of model components and water movement

170 The moisture content and salt content are calculated for each day (Fig.1). All flow
171 takes place within the day and the water and salt content are in “equilibrium” (i.e.,
172 fluxes are zero) at the end of the day for which the calculations are made. Daily fluxes
173 considered in the vadose model are the following: at the surface, the fluxes are
174 irrigation, both irrigation water, $I(t)$, and salt, $S_o(t)$, and precipitation, $P(t)$, and for each
175 layer, j , on days with irrigation and rainfall, the downward flux of water, $R_w(j,t)$, and salt,
176 $S(j,t)$, between the layers. On days without water input at the soil surface, an upward
177 groundwater flux $U(j,h,t)$, and salt, $S(j,t)$ are considered. The flux to the surface
178 depends on the groundwater depth. Finally, transpiration, $T(j,t)$, removes water from
179 the layers with roots of the crops and evaporation, $E(j,t)$, from all layers.

180 The EPICS model consists of two modules: the VADOSE module and the CROP
181 module. The two modules are linked through the evapotranspiration flux in the soil
182 (Fig. 2).



183

184 Fig 2. Schematic diagram of the linked novel Shallow Aquifer-Vadose zone surrogate
 185 module and EPIC module. Note: ET_0 is the reference evapotranspiration, E_p and T_p
 186 are the potential evaporation and potential transpiration, E_a and T_a are the actual
 187 evaporation and actual transpiration, K_c is the crop coefficient, τ is the development
 188 stage of the leaf canopy, and r_j is the root function of soil layer j .

189

190 The CROP module employs functions of the EPIC model (Williams et al., 1989)
 191 and root growth distribution (Novak, 1987; Kendy et al., 2003; Chen et al. 2019). The
 192 CROP module calculates daily values of crop height, root depth and leaf area index
 193 (LAI) based on climatic data (Fig. 2).

194 The VADOSE module calculates the moisture and salt content in the root zone
 195 and the upward movement of the groundwater (Fig.2). Field capacity varies with
 196 depth and is a function of the (shallow) groundwater depth and the soil characteristic
 197 curve (Liu et al., 2019). Moisture contents become less than field capacity when the

198 upward flux is less than the actual evapotranspiration.

199 Finally, the link between the VADOSE and the CROP modules is achieved by
200 calculating the actual evapotranspiration with parameters of both modules consisting
201 of the moisture content and the salt content simulated in the VADOSE module and
202 root distribution and potential evapotranspiration in the CROP module (Fig. 2).

203 2.3 Theoretical background of the EPICS model

204 In the next section, the equations of the CROP in the VADOSE modules are
205 presented. The calculations are carried out sequentially on a daily time step. This
206 model predicts field daily soil water, salt content and crop growth, which are critical
207 parameters for irrigation water management. For field and regional water
208 management and irrigation policy development, resolution of daily time step is
209 sufficient. Finer resolution is not needed for managing water and salt content for
210 irrigation. In the first step, the actual evaporation and transpiration are calculated for
211 each layer in the model. Next, the moisture content and salt content are adjusted for
212 the various fluxes. Since the equations for the downward movement on days of
213 rainfall and/or irrigation are different than for upward movement from the groundwater
214 on the remaining days, we present upward and downward movement in separate
215 sections. The code was written in Matlab 2014Ra and Microsoft Excel was used for
216 data input and output.

217 2.3.1 CROP module

218 The crop module uses functions of EPIC (Erosion Productivity Impact Calculator,

219 Williams et al., 1989) to calculate leaf area index, LAI, crop height and the root depth
 220 (green boxes in Fig. 2), and the potential transpiration, T , and evaporation, E (orange
 221 boxes in Fig, 2). Input data for the CROP module included: mean daily temperature
 222 (T_{mean}), maximum daily temperature (T_{mx}), minimum daily temperature (T_{mn}),
 223 maximum crop height (H_{mx}), maximum LAI (LAI_{mx}), maximum root depth (RD_{mx}),
 224 dimensionless canopy extinction coefficient (K_b), and total potential heat units
 225 required for crop maturation (PHU).

226 The potential rates of evaporation, $E_p(j, t)$, and transpiration, $T_p(j, t)$, of different
 227 layers are derived from the total rates and a root function that determines the
 228 distribution of roots in the vadose zone

$$229 \quad T_p(j, t) = r_T(j, t)T_p(t) \quad (1a)$$

$$230 \quad E_p(j, t) = r_E(j, t)E_p(t) \quad (1b)$$

231 where j is the number of soil layers and t is the day number, $T_p(t)$ is the total
 232 potential transpiration and $E_p(t)$ is the total potential transpiration at time, t . Both are
 233 calculated with the CROP module (S1 in the supplementary material). Root functions
 234 (Sau et al., 2004; Delonge et al., 2012) were used to calculate transpiration and
 235 evaporation of different soil layer. $r_T(j, t)$ is the root function for the transpiration and
 236 $r_E(j, t)$ is the root function for the evaporation. Both have the same general equation
 237 but with a different value for the constant δ .

$$238 \quad r_T(j, t) = \left[\frac{1}{1 - \exp(-\delta)} \right] \left\{ \exp \left[-\delta \left(\frac{Z_{1j}}{Z_{2j}} \right) \right] \left[1 - \exp \left(-\delta \frac{Z_{2j} - Z_{1j}}{Z_r} \right) \right] \right\} \quad (2a)$$

$$239 \quad r_E(j, t) = \left[\frac{1}{1 - \exp(-\delta)} \right] \left\{ \exp \left[-\delta \left(\frac{Z_{1j}}{Z_{2j}} \right) \right] \left[1 - \exp \left(-\delta \frac{Z_{2j} - Z_{1j}}{Z_r} \right) \right] \right\} \quad (2b)$$

240 Where z_{1j} is the depth of the upper boundaries of the soil layer j . For $r_T(j, t)$ if the
 241 root depth is smaller than the lower boundaries of the soil layer j , Z_{2j} is equal to the
 242 root depth and if the root depth is greater than the lower boundaries of the soil layer j ,
 243 Z_{2j} is the depth of the lower boundaries of the soil layer j . For $r_E(j, t)$, Z_{2j} is depth of
 244 the lower boundaries of the soil layer j . Z_r is the root zone depth and δ is the water
 245 use distribution parameter. Note that the sum of $r_T(j, t)$ of all soil layers is equal to 1.
 246 In the study of Novark (1987), the value of δ for corn is 3.64 and we used this value.
 247 To obtain $r_E(j, t)$, δ was set to 10 (Chen et al., 2019; Kendy et al., 2003). Sunflower
 248 root function simulation employed the same δ values as for maize.

249 The actual evaporation rates, $E_a(j, t)$, and transpiration, $T_a(j, t)$, for each soil
 250 layer, j , at time, t , are calculated as a proportion of the potential values as:

$$251 \quad E_a(j, t) = k_E(j, t)E_p(j, t) \quad (3a)$$

$$252 \quad T_a(j, t) = k_T(j, t)S(j, t)T_p(j, t) \quad (3b)$$

253 where $k_E(j)$ and $k_T(j)$ are water stress coefficients and $S(j)$ is a salt stress
 254 coefficient. According to Raes et al. (2009), the water stress coefficients are

$$255 \quad k_E(j, t) = \exp\left(-2.5 \frac{\theta_{fc}(j) - \theta(j, t)}{\theta_{fc}(j) - \theta_r(j)}\right) \quad \theta \leq \theta_{fc} \quad (4a)$$

$$256 \quad k_E(j, t) = 1 \quad \theta > \theta_{fc} \quad (4b)$$

257 where $\theta_{fc}(j)$ is the moisture content at field capacity for layer j , or when the
 258 conductivity becomes limiting and $\theta_r(j)$ is the moisture content at wilting point,
 259 $\theta(j, t)$ is the soil moisture content for layer j at time t .

260 Then water stress coefficient in Eq. 3b is:

$$k_T(j, t) = 1 - \frac{\exp\left[\left(1 - \frac{\theta(j, t) - \theta_r(j)}{(1-p)[\theta_{fc}(j) - \theta_r(j)]}\right) f_{shape}\right] - 1}{\exp(f_{shape}) - 1} \quad \theta \leq \theta_{fc} \quad (5a)$$

$$k_T(j, t) = 1 \quad \theta > \theta_{fc} \quad (5b)$$

where f_{shape} is the shape factor of $k_T(j, t)$ curve, p is the fraction of readily available soil water relative to the total available soil water. Finally, the salt stress coefficient $S(j, t)$ for each layer in Eq 3b can be calculated as (Allen et al., 1998; Xue et al., 2018):

$$S(j, t) = 1 - \frac{B}{100 k_y} (EC_e(j, t) - EC_{threshold}) \quad (6)$$

where k_y is the factor that affects the yield, EC_e is the electrical conductivity of the soil saturation extract (mS cm^{-1}), $EC_{threshold}$ is the calibrated threshold of the electrical conductivity of the soil saturation extract when the crop yield becomes affected by salt (mS cm^{-1}), and B is the calibrated crop specific parameter that describes the decrease rate of crop yield when EC_e increases per unit below the threshold. The electrical conductivity of the soil saturation extract can be calculated as (Rhoades et al., 1989):

$$EC_e = 1.33 + 5.88 \times EC_{1:5} \quad (7)$$

where $EC_{1:5}$ is the electrical conductivity of the soil extract that soil samples mixed with distilled water in a proportion of 1:5.

2.3.2 VADOSE Module

For modeling the daily soil moisture content and groundwater depth, first we need to calculate the soil moisture content at field capacity and the drainable porosity based on the soil moisture characteristic curve. Besides, we assume that the water and salt

282 moves downward on rainy and/or irrigation days, while the water and salt moves
283 upward on days without rain and/or irrigation.

284 2.3.2.1 Parameters based on soil moisture characteristic curve for modeling

285 Moisture content at field capacity

286 Field capacity with a shallow groundwater is different than in soils with deep
287 groundwater where water stops moving when the hydraulic conductivity becomes
288 limiting at -33 kPa. When the groundwater is shallow, the hydraulic conductivity is not
289 limiting and the water stops moving when the hydraulic potential is constant and thus
290 the matric potential is equal to the height above the water table (Gardner 1958;
291 Gardner et al., 1970a, b; Steenhuis et al. 1988; Liu et al., 2019). Assuming a unique
292 relationship between moisture content at field capacity and matric potential (i.e. soil
293 characteristic curve), the moisture content at field capacity at any point above the
294 water table is a unique function of the water table depth. Thus, any water added
295 above field capacity will drain downward. When the groundwater is recharged, the
296 water table will rise and increase the moisture contents at field capacity throughout
297 the profile.

298 The moisture contents at field capacity were found by Liu et al. (2019) using the
299 simplified Brooks and Corey soil characteristic curve (Brooks and Corey, 1964)

$$300 \quad \theta = \theta_s \left[\frac{\varphi_m}{\varphi_b} \right]^{-\lambda} \quad \text{for } |\varphi_m| > |\varphi_b| \quad (8a)$$

$$301 \quad \theta = \theta_s \quad \text{for } |\varphi_m| \leq |\varphi_b| \quad (8b)$$

302 in which θ is the soil moisture content ($\text{cm}^3 \text{ cm}^{-3}$), θ_s is the saturated moisture

303 content ($\text{cm}^3 \text{ cm}^{-3}$), φ_b is the bubbling pressure (cm), φ_m is matric potential (cm),
 304 and λ is the pore size distribution index. The moisture content at field capacity,
 305 $\theta_{fc}(z, h)$, for any point, z , from the surface water for a groundwater at depth, h , can be
 306 expressed as (Liu et al. 2019)

$$307 \quad \theta_{fc}(z, h) = \theta_s(z) \left[\frac{h - z}{\varphi_b} \right]^{-\lambda} \quad \text{for } |h - z| > |\varphi_b(z)| \quad (9a)$$

$$308 \quad \theta_{fc}(z, h) = \theta_s(z) \quad \text{for } |h - z| \leq |\varphi_b(z)| \quad (9b)$$

309 where h (cm) is the depth of the groundwater and z (cm) is the depth of the point
 310 below the soil surface. Thus $(h-z)$ is the height above the groundwater and this is
 311 equal to the matric potential for soil moisture content at field capacity.

312 For shallow groundwater, the matric potential at the surface is -33kPa when the
 313 groundwater is 3.3 m depth. For this matric potential, as mentioned above, the
 314 conductivity becomes limiting. This depth of the groundwater is therefore the lower
 315 limit over which the VADOSE module is valid.

316 Evapotranspiration can lower the soil moisture content below field capacity. Thus,
 317 the maximum moisture content in the VADOSE module is determined by the soil
 318 characteristic curve and the height of the groundwater table, and the minimum is the
 319 wilting point that can be obtained by evapotranspiration by the crop. Note that the
 320 saturated hydraulic conductivity does not play a role in determining the moisture
 321 content because inherently it is assumed that it is not limiting in the distribution of the
 322 water.

323 Drainable porosity

324 The drainable porosity is a crucial parameter in modelling the groundwater depth and
 325 soil moisture content. According to the soil water characteristic curve at field capacity,
 326 the drainable porosity can be expressed as a function of the depth. The drainable
 327 porosity is obtained by calculating the field capacity, $W_{fc}(h)$ (cm) for each layer at all
 328 groundwater depths. The total water content at field capacity of the soil profile over a
 329 prescribed depth with a water table at depth h can be expressed as:

$$330 \quad W_{fc}(h) = \sum_{j=1}^n [L(j) \theta_{fc}(j, h)] \quad (10)$$

331 where $\theta_{fc}(j, h)$ is the average moisture content at field capacity of layer j that can be
 332 found by integrating Eq. 8 from the upper to the lower boundary of the layer and
 333 dividing by the length $L(j)$ which is the height of layer j . The matric potential at the
 334 boundary is equal to the height above the water table. The drainable porosity, $\mu(h)$,
 335 which is a function of the groundwater depth h , can simply be found as the difference
 336 in water content when the water table is lowered over a distance of $2\Delta h$.

$$337 \quad \mu(h) = \frac{W_{fc}(h + \Delta h) - W_{fc}(h - \Delta h)}{2\Delta h} \quad (11)$$

338 where $\Delta h = 0.5L(j)$ (cm).

339 2.3.2.2 Downward flux (at times of irrigation and/or precipitation) and model output

340 During the downward flux period, the upward water flux from groundwater is zero.

341 Under this condition, the model can output the daily soil moisture content of different
 342 soil layers, the percolation from each soil layer to the soil layer beneath, the discharge
 343 from soil water to groundwater, the salt concentration of groundwater and of soil water
 344 in each soil layer, and the groundwater depth.

345 **Water**

346 A downward flux occurs when either the precipitation or irrigation is greater than the
347 actual evapotranspiration. In this case, upward flux will not occur because the actual
348 evapotranspiration is subtracted from the input at the surface. We consider two cases
349 when the groundwater is being recharged and when it is not.

350 When the net flux at the surface (irrigation plus rainfall minus actual
351 evapotranspiration) is greater than that needed to bring the soil up to equilibrium
352 moisture content, the groundwater will be recharged and the distance of the
353 groundwater to soil surface decreases and the moisture content will be equal to the
354 moisture at field capacity. The fluxes from one layer to the next can be calculated
355 simply by summing the amount of water needed to fill up each layer below to the new
356 moisture content at field capacity. Hence, the percolation to groundwater, $R_{gw}(t)$, can
357 be expressed as:

358
$$R_{gw}(t) = P(t) + I(t) - E_a(t) - T_a(t) - \sum_{j=1}^n \frac{[\theta_{fc}(j, h) - \theta(j, t - \Delta t)]L(j)}{\Delta t} \quad (12)$$

359 where n is the total number of layers, $\theta(j, t)$ is the average soil moisture content in
360 day t of layer j ($\text{cm}^3 \text{cm}^{-3}$), $E_a(t)$ is the actual evaporation (mm), $T_a(t)$ is the actual
361 transpiration (mm), $P(t)$ is the precipitation (mm), and $I(t)$ is the irrigation (mm).

362 When the groundwater is not recharged, the rainfall and the irrigation are added
363 to uppermost soil layer and when the soil moisture content will be brought up to the
364 field capacity and the excess water will infiltrate to next soil layer bringing it up to field
365 capacity. This process continues until all the rainwater is distributed. Formally the soil
366 moisture can be expressed as

367
$$\theta(j, t) = \min \left[\theta_{fc}(j, h), \left[\theta(j, t - \Delta t) + \frac{R_w(j-1, t) \Delta t}{L(j)} \right] \right] \quad (13)$$

368 where $\theta(j, t)$ is the average soil moisture content in day t of layer j ($\text{cm}^3 \text{cm}^{-3}$),
 369 $R_w(j - 1, t)$ is the percolation rate to layer j (mm) and can be found with Eq 12 by
 370 replacing $j-1$ for n in the summation sign.

371
$$R_w(j - 1, t) = P(t) + I(t) - E_a(t) - T_a(t) - \sum_1^{j-1} \frac{[\theta_{fc}(j, h) - \theta(j, t - \Delta t)]L(j)}{\Delta t} \quad (14)$$

372 For the uppermost soil layer, the water percolation can be expressed as

373
$$R_w(0, t) = I(t) + P(t) - E_a(t) - T_a(t) \quad (15)$$

374 **Salinity**

375 The salt concentration for layer j can be expressed by a simple mass balance as:

376
$$C(j, t) = \frac{\theta(j, t - \Delta t) C(j, t - \Delta t)L(j) + [R_w(j - 1, t) C(j - 1, t) - R_w(j, t) C(j, t)] \Delta t}{\theta(j, t)L(j)} \quad (16)$$

377 where $C(j, t)$ is the salt concentration of layer j at time t (g L^{-1}). The equation can be
 378 rewritten as an explicit function of $C(j, t)$

379
$$C(j, t) = \left[\frac{\theta(j, t)L(j)}{1 + R_w(j, t) \Delta t} \right] \left[\frac{\theta(j, t - \Delta t) C(j, t - \Delta t)L(j) + R_w(j - 1, t) C(j - 1, t) \Delta t}{\theta(j, t)L(j)} \right] \quad (17)$$

380 For the surface layer $j=1$, we obtain

381
$$C(1, t) = \left[\frac{\theta(1, t)L(1)}{1 + R_w(1, t)\Delta t} \right] \left[\frac{\theta(1, t)L(1)}{1 + R_w(1, t)\Delta t} \frac{\theta(j, t - \Delta t) C(j, t - \Delta t)L(j) + I(t) C_i \Delta t}{\theta(j, t)L(j)} \right] \quad (18)$$

382 where C_i is the salt concentration in the irrigation water (g L^{-1}).

383 The salt concentration of the groundwater $C_{gw}(t)$ can be estimated as:

384
$$C_{gw}(t) = \frac{[G(t - 1) \times C_{gw}(t - 1) + C(5, t) \times R_w(t)]}{G(t - 1) + R_w(t)} \quad (19)$$

385 Where $C(5, t)$ is the soil salinity concentration of the soil layer 5 on day t (g L^{-1}),
 386 $G(t - 1)$ is the difference of the groundwater depth and the depth that the largest
 387 groundwater table fluctuations depth of groundwater table on day $(t-1)$ (m) (Xue et al.,

388 2018), $C_{gw}(t)$ is the soluble salt concentration of groundwater at day t (g L^{-1}).

389 2.3.2.3 Upward flux and model output

390 For the upward flux period, the downward water flux to groundwater is zero. The
391 evapotranspiration leads to the decrease of soil moisture content in the vadose zone
392 and lowers the groundwater table due to the upward movement of groundwater to
393 crop root zone and soil surface. The soil moisture content is calculated by taking the
394 difference of equilibrium moisture content associated with the change of groundwater
395 depth. Under this condition, the model can output the daily soil moisture content of
396 different soil layers, the upward groundwater flux, the groundwater depth, and the salt
397 concentration of groundwater and of soil water in each soil layer.

398 **Water**

399 The groundwater upward flux, $U_{gw}(h, t)$, is limited by either the maximum upward
400 flux of groundwater, $U_{gw,max}(h)$, or the actual evapotranspiration, formally stated as:

$$401 \quad U_{gw}(h, t) = \min [[E_a(t) + T_a(t)], U_{gw,max}(h)] \quad (20)$$

$$402 \quad E_a(t) = \sum_{j=1}^n E_a(j, t) \quad (21)$$

$$403 \quad T_a(t) = \sum_{j=1}^n T_a(j, t) \quad (22)$$

404 where $U_{gw,max}(h)$ is the actual upward flux from groundwater (mm), $E_a(t)$ is the
405 actual evaporation at day t (mm), $T_a(t)$ is the actual transpiration at day t (mm),
406 $E_a(j, t)$ is the actual evaporation at day t of layer j (mm) and $T_a(j, t)$ is the actual
407 transpiration at day t of layer j (mm).

408 The maximum upward flux can be expressed as (Liu et al., 2019; Gardner et al.,

409 1958)

$$410 \quad U_{gw,max}(h) = \frac{a}{e^{bh} - 1} \quad (23)$$

411 where a and b are constants that need to be calibrated, h is the groundwater depth
412 (cm).

413 Two cases are considered for determining the moisture contents of the layers
414 depending on whether the actual evapotranspiration is greater or less than the
415 maximum upward flux.

416 Case I: $U_{gw,max}(h) > E_a(t) + T_a(t)$

417 In this case, where the maximum upward flux is greater than the evaporative demand,
418 the groundwater depth is updated

$$419 \quad h(t) = h(t - \Delta t) + \frac{E_a(t) + T_a(t)}{\mu(\bar{h})} \quad (24)$$

420 where $\mu(\bar{h})$ is the average drainable porosity over the change in groundwater depth
421 h . The moisture content after the change in groundwater depth becomes

$$422 \quad \theta(j, t) = \theta(j, t - \Delta t) + \theta_{fc}(j, h(t)) - \theta_{fc}(j, h(t - \Delta t)) \quad (25)$$

423 Note that when the layer is at field capacity and the upward flux is equal to the
424 evaporative flux, the layer remains at field capacity for the updated groundwater
425 depth at time t .

426 Case II: $U_{gw,max}(h) \leq E_a(t) + T_a(t)$

427 In this case, the groundwater depth is updated

$$428 \quad h(t) = h(t - \Delta t) + \frac{U_{gw,max}(h)}{\mu(\bar{h})} \quad (26)$$

429 When the upward flux is less than the sum of the actual evaporation and transpiration,

430 the moisture content is updated with the difference between the two fluxes,
 431 $U_{gw,max}(h)$ and $[E_a(t) + T_a(t)]$, according to a predetermined distribution extraction of
 432 water out of the root zone

$$433 \theta(j, t) = \theta(j, t - \Delta t) + \theta_{fc}(j, h(t)) - \theta_{fc}(j, h(t - \Delta t)) - \frac{r(j)[E_a(t) + T_a(t) - U_{gw,max}(h)]}{L(j)} \quad (27)$$

434 The upward flux of water can be found by summing the differences in moisture
 435 content above the layer j similar to Eq 14, but starting the summation at the
 436 groundwater.

437 Salinity

438 The salt from groundwater is added to the soil layers according to the root function.

439 The soil salinity concentration in layer j at day t can be expressed as

$$440 C(j, t) = \frac{\theta(j, t - \Delta t) C(j, t - \Delta t) L(j) + r(j, t) U_g(h, t) C_{gw}(t)}{\theta(j, t - \Delta t) L(j) + (\theta_{fc}(j, h(t)) - \theta_{fc}(j, h(t - \Delta t))) L(j) - r(j, t) (E_a(t) + T_a(t) - U_{gw,max}(h))} \quad (28)$$

441 Since water is extracted from the reservoir that has the same concentration as in the
 442 reservoir, the concentration will not change, hence the equation used to estimate the
 443 groundwater salt concentration can be expressed as

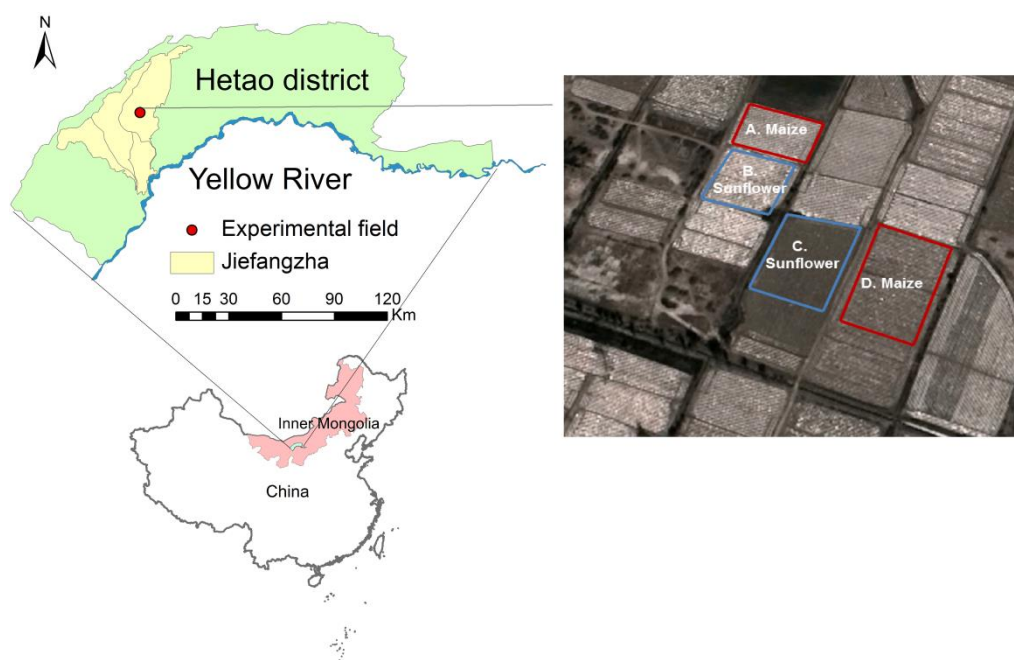
$$444 C_{gw}(t) = C_{gw}(t - \Delta t) \quad (29)$$

445 3. Data collection

446 3.1 Study area

447 Field experiments were conducted in 2017 and 2018 in Shahaoqu experimental
 448 station in Jiefangzha sub-district, Heato irrigation district in Inner Mongolia, China (Fig.
 449 3). Irrigation water originates from the Yellow River. [The change of the irrigation water](#)
 450 [salinity is small and can be ignored during the crop growth period.](#) The area has an
 451 arid continental climate. Mean annual precipitation is 155 mm a⁻¹ of which 70% falls

452 from June to September. Pan evaporation is 2000 mm a⁻¹ (Xu et al., 2010). The mean
453 annual temperature is 7°C. The soils begin to freeze in the middle of November and to
454 thaw in end of April or beginning of May. Maize, wheat and sunflower are the main
455 crops in Jiefangzha sub-district and are grown with flood irrigation. The groundwater
456 depth is between 0.5-3 m. Regional exchange of groundwater is minimal due to low
457 gradient of 0.01-0.025 (Xu et al., 2010). Thus, the groundwater flows mainly vertically
458 with minimum lateral flow in the regional scale. Over 50% of the total irrigated
459 cropland, 5250 km² in the Hetao irrigation district in the Yellow River basin, is affected
460 by salinity (Feng et al., 2005).



461
462 Fig. 3 Location of the Shahaoqu experimental field (Note: The figure was downloaded
463 from Google earth. The imagery is taken on April 8, 2019)

464 3.2 Field observations and data

465 The layout of the experimental fields is shown in Figure 3. The areas of fields A, B, C
466 and D are 920, 2213, 1167, 1906 m², respectively. Field A and D were planted with

467 maize on May 10 and harvested on September 30, 2017. In 2018, fields A and D were
 468 planted with gourds and were therefore not monitored in 2018. Fields B and C were
 469 seeded with sunflower in both 2017 and 2018. The sunflower was planted on June 1,
 470 2017 and June 5, 2018. Harvest was on September 15 in both years. The fields were
 471 irrigated by flooding the field ranging from two to five times during the growing season
 472 (Table 1). The salinity of the irrigation source water was measured three times during
 473 crop growth period and the mean value was used in the mass balance. The salinity of
 474 the irrigation source water is assumed unchanged. A well was installed in each
 475 experimental field to monitor the groundwater depth.

476 Table 1 Irrigation scheduling for the Shahaoqu experimental fields in 2017 and 2018

Field	Year	Irrigation events	Date	Irrigation depth (mm)
A (maize)	2017	1	5/30	100
		2	6/25	162
		3	7/14	275
		4	8/6	199
B (sunflower)	2017	1	6/26	140
		2	7/23	121
	2018	1	6/20	134
		2	6/24	60
		3	7/15	114
C (sunflower)	2017	4	7/22	40
		5	8/31	130
	2018	1	6/19	80
		2	6/30	80
D (maize)	2017	1	6/20	140
		2	7/14	100
		1	6/13	150
		2	6/26	94
		3	7/6	50
4	7/14	174		
5	8/6	120		

477

478 Daily meteorological data, including air temperature, precipitation, relative
479 humidity, wind speed, and sunshine duration, originated from the weather station at
480 the Shahaoqu experimental station. The soil moisture content for the four
481 experimental fields in 2017 and for field C in 2018 during the crop growing season
482 was measured every 7-10 days at the depths of 0-20, 20-40, 40-60, 60-80, 80-100 cm
483 by taking soil samples and oven drying. In 2018, in addition, the soil moisture content
484 at same depths was monitored daily using Hydra Probe Soil Sensors (Stevens Water
485 Monitoring System Inc., Portland, OR, USA) in field B except the oven drying method.
486 The Hydra Probe was calibrated using the intermittent manual measurements. In
487 2017, the groundwater depths were manually measured in all four experimental fields
488 about every 7-10 days. In 2018, the groundwater depth in fields B and C was
489 recorded at 30 min intervals using an HOBO Water Level Logger-U20 (Onset, Cape
490 Cod, MA, USA). The sensors of the soil moisture content and groundwater depth
491 were connected to data loggers and downloaded via wireless transmission. The crop
492 leaf area and crop height were manually measured every 7-12 days.

493 Undisturbed soil samples were collected in 5 cm high rings with a diameter of 5.5
494 cm from the five soil layers where the soil moisture were taken and used for textual
495 analysis, saturated soil moisture content, field capacity and soil bulk density. The soil
496 texture was analyzed with a laser particle size analyzer (Mastersizer 2000, Malvern
497 Instruments Ltd., United Kingdom). The American soil texture classification method
498 was used in this study. Finally, the soil samples were collected 7-10 days apart to
499 monitor the change of electrical conductivity (EC). The soil samples were mixed with

500 distilled water in a proportion of 1:5 to measure the electrical conductivity of the soil
501 water by a portable conductivity meter. It is assumed that 1 ms cm^{-1} corresponds to
502 640 mg L^{-1} of total dissolved salts (Wallender and Tanji, 2011; Xue et al., 2018).

503 3.3 Model calibration and validation

504 The observed soil moisture contents, groundwater depths, crop heights, LAIs and
505 salinity concentrations for field A with maize and sunflower fields B and C in 2017
506 were used for calibration and the sunflower data of fields B and C in 2018 and the
507 maize data in field D in 2017 were used for validation. The initial θ_{fc} was based on the
508 measured data (Table 2). The initial values of θ_s and θ_r were derived from the soil
509 texture with the method of Ren et al. (2016) (Table2). The default values of EPIC for
510 sunflower and maize were used as initial values for simulating crop growth (K_{cmax} and
511 LAI_{mx} in Eq. S3, K_b in Eq. S4, H_{mx} in Eq. S7, PHU in Eq. S9, T_b in Eq. S10, ad in Eq.
512 S12, T_0 and T_b in Eq. 16, RD_{mx} in Eq. S18). The initial value maximum crop coefficient
513 (K_{cmax}) in Eq. S3 in Supplementary S1 for evapotranspiration calculation was taken
514 from *Sau et al.*, (2004). The initial values of two groundwater parameters (a and b in
515 Eq. 23) were based on Liu et al., (2019). The Brooks and Corey soil moisture
516 characteristic parameters (φ_b , λ in Eq. 8) were obtained by fitting the outer envelope
517 of the measure moisture content and water table data.

518 Statistical indicators were used to evaluate goodness of fit of the hydrological
519 model for both calibration and validation (Ritter and Muñoz-Carpena, 2013). The
520 statistical indicators included the root mean square error (RMSE) (Abrahart and See,
521 2000),

522
$$\text{RMSE} = \sqrt{\frac{1}{N} \sum_{i=1}^N (P_i - O_i)^2}$$
 (30)

523 the mean relative error (MRE) (Dawson et al., 2006; Nash and Suscliff, 1970),

524
$$\text{MRE} = \frac{1}{N} \sum_{i=1}^N \frac{(P_i - O_i)}{O_i} \times 100\%$$
 (31)

525 the Nash-Sutcliffe efficiency coefficient (NSE) (Nash and Suscliff, 1970),

526
$$\text{NSE} = 1 - \frac{\sum_{i=1}^N (P_i - O_i)^2}{\sum_{i=1}^N (O_i - \bar{O})^2}$$
 (32)

527 and the determination coefficient (R^2) and regression coefficient (b) (Xu et al., 2015)

528
$$R^2 = \left[\frac{\sum_{i=1}^N (O_i - \bar{O})(P_i - \bar{P})}{[\sum_{i=1}^N (O_i - \bar{O})]^{0.5} [\sum_{i=1}^N (P_i - \bar{P})]^{0.5}} \right]^2$$
 (33)

529
$$b = \frac{\sum_{i=1}^N O_i \times P_i}{\sum_{i=1}^N O_i^2}$$
 (34)

530 where N is the total number of observations; P_i and O_i are the i^{th} model predicted and
 531 observed values ($i=1,2,3\dots N$), respectively; \bar{O} and \bar{P} are the mean observed values
 532 and predicted values, respectively. The RMSE is used to evaluate the bias of the
 533 measured data and predicted data. The MRE can evaluate the credibility of the
 534 measured data. The NSE is usually used to evaluate the quality of the hydrological
 535 models. The R^2 is used to measure the fraction of the dependent variable total
 536 variation that can be explained by the independent variable. And the regression
 537 coefficient represents the influence of the independent variable on the dependent
 538 variable in the regression equation. The value of RMSE and MRE close to 0 indicates
 539 good model performance. The value of NSE ranges from $-\infty$ to 1. NSE=1 means a
 540 perfect fit while the negative NSE value indicates the mean observed value is a better

541 predictor than the simulated value (Moriasi et al., 2007). For b and R², the value
542 closest to 1 indicates good model predictions.

543 3.4 Parameters sensitivity analysis

544 A sensitivity analysis was performed to determine how the input parameters
545 affected output of the models (Cloke et al., 2008; Cuo et al., 2011). Each parameter
546 was varied over a range of -30% to 30% to derive the corresponding impact on the
547 model output of soil moisture, groundwater depth, soil salinity, leaf area index and
548 actual evapotranspiration. The change in output values was plotted against the
549 change in input values.

550 4 Results

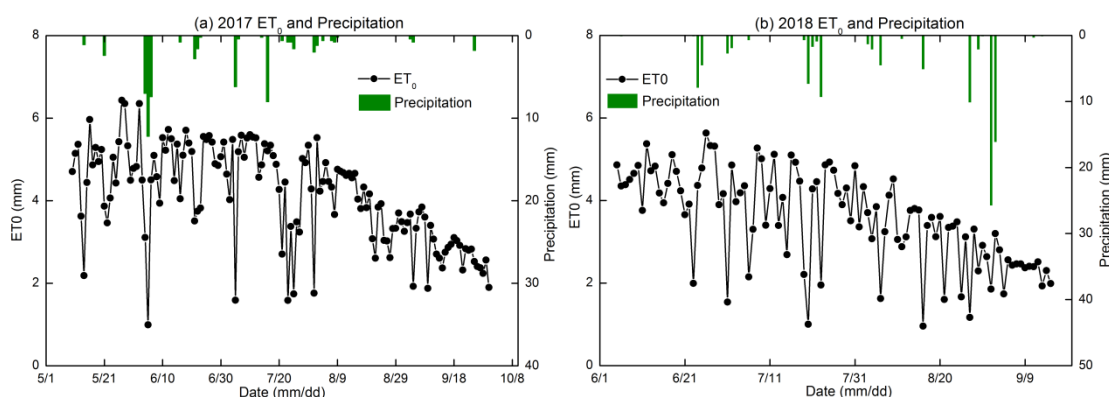
551 The 2017 and 2018 experimental data of the Shahaoqu farmers' fields in the
552 Hetao irrigation district (Fig.3) are presented first, followed by the calibration and
553 validation results of the CROP and VADOSE modules of EPICS model.

554 4.1 Results of the field experiment

555 4.1.1 Water input

556 The precipitation was 63 mm in 2017 (May 10 to September 30) and 108 mm in
557 2018 (June 1 to September 15). The precipitation from the greatest rainstorm was 26
558 mm on September 1, 2018 (Fig. 4). Irrigation provided most of the water for the crops.
559 Field A (maize) was irrigated four times with a total of 736 mm and field D (maize) was
560 irrigated five times for a total of 588 mm in 2017. Sunflower fields B and C were both
561 irrigated twice with a total water amount of 261mm and 160mm, respectively, in 2017.
562 In 2018, fields B and C were irrigated five and two times, respectively, with a total

563 water amount of 478mm and 240mm, respectively. The reference evapotranspiration
 564 ranged from 1 mm d⁻¹ to a maximum of 6.4 mm d⁻¹ during crop growing period (Fig. 4).
 565 The total reference evapotranspiration from May 10 to September 30, 2017 was 595
 566 mm and 368 mm from June 1 to September 15, 2018. The reason was that there
 567 were more rainfall days in June, July and September in 2018 than in 2017, which
 568 increased the amount of water available for the evapotranspiration by the crop in
 569 2018. In addition, the wind speed was high in May that increase the
 570 evapotranspiration was elevated. In the study of Ren et al. (2017) and Miao (et al.
 571 2016), the mean ET₀ was over 6 mm per day on May. Hence, the ET₀ during the study
 572 period in 2017 was greater than in 2018.



573
 574 Fig 4. Reference evapotranspiration (ET₀) and precipitation during crop growth period
 575 in 2017 and 2018.

576
 577 4.1.2 Soil physical properties

578 Based on the soil textural analysis in Table 2, the soils were classified as silt, silt loam
 579 and loamy sand. Bulk densities varied from 1.24 to 1.47 Mg m⁻³ with the greatest bulk
 580 densities in the 0-20 cm soil layer. There was generally more sand in the top 40 cm
 581 than below. The subsoil was heavier and had the greatest percentage of silt (Table 2).

582 The moisture content at -33 kPa (0.33 bar) varied from 0.25 to 0.35 cm³cm⁻³ and at
 583 1.5Mpa (wilting point at 15 bar) ranged from 0.08 to 0.15 cm³cm⁻³ (Table 2).

584 Table 2 Soil texture and bulk density of the experimental fields in Shahaoqu

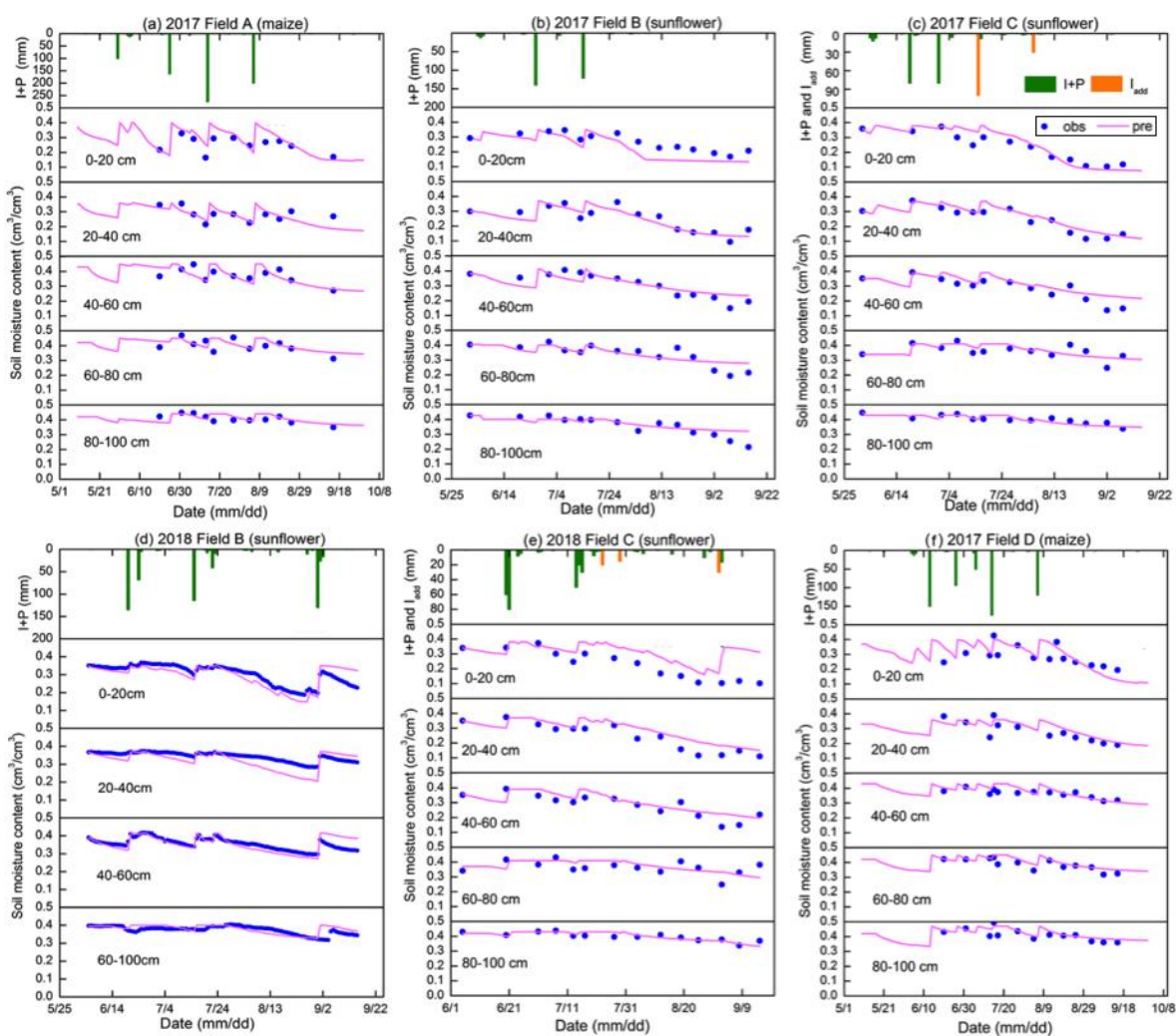
Field	Soil depth (cm)	Sand(%)	Silt(%)	Clay(%)	Soil type	ρ (Mg m ⁻³)	θ_{fc} (m ³ m ⁻³)	θ_r (m ³ m ⁻³)
A	0-20cm	26	62	13	Silt loam	1.44	0.31	0.1
	20-40cm	76	22	2	Loamy sand	1.24	0.32	0.07
	40-60cm	10	79	10	Silt loam	1.33	0.33	0.12
	60-100cm						0.34	0.14
			6	79	15	Silt loam	1.35	0.35
B	0-20cm	22	64	13	Silt loam	1.44	0.29	0.15
	20-40cm	16	73	11	Silt loam	1.24	0.26	0.13
	40-60cm	18	73	9	Silt loam	1.33	0.32	0.11
	60-80cm	8	77	16	Silt	1.35	0.34	0.14
	80-100cm	13	79	8	Silt loam		0.35	0.12
C	0-20cm	29	63	8	Silt loam	1.47	0.26	0.08
	20-40cm	37	56	6	Silt loam	1.33	0.25	0.08
	40-60cm	35	59	7	Silt loam	1.32	0.26	0.08
	60-80cm	14	74	12	Silt loam	1.38	0.31	0.12
	80-100cm	10	82	8	Silt	1.38	0.34	0.11
D	0-20cm	27	62	11	Silt loam	1.47	0.3	0.15
	20-40cm	5	80	15	Silt loam	1.33	0.27	0.14
	40-60cm	7	75	18	Silt loam	1.32	0.33	0.15
	60-100cm						0.34	0.12
		10	81	9	Silt	1.38	0.31	0.14

585

586 4.1.3 Soil moisture content

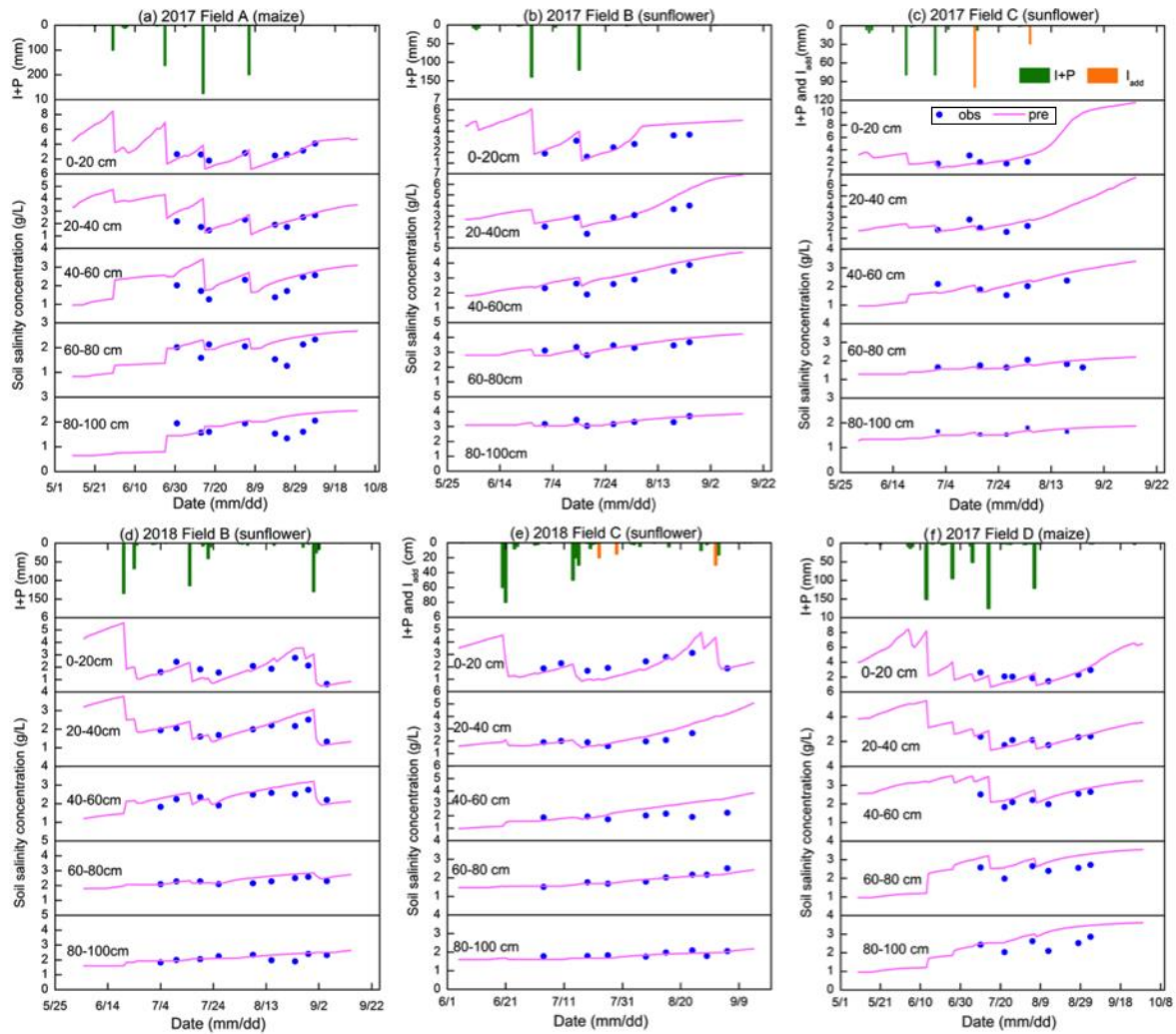
587 Moisture content, rainfall and irrigation amounts are depicted for the five layers
 588 and the four fields in 2017 and two fields in 2018 in Fig. 5. Blue closed spheres
 589 indicate that the moisture content was determined on cored soil samples (Figs. 5a, b,
 590 c, e, f) and close-spaced spheres when the hydra probe was used (Fig. 5d). The
 591 moisture contents were near saturation when irrigation water was added and

592 subsequently decreased due to crop transpiration and soil evaporation (Fig. 5). In all
 593 cases, the moisture contents during the main growing period remained above the
 594 moisture content at -33 kPa that ranged from 0.25 $\text{cm}^3\text{cm}^{-3}$ to 0.34 $\text{cm}^3\text{cm}^{-3}$ for the
 595 60-80 cm depth (Table 2, Fig.5). Only after the last irrigation and during harvest of the
 596 crop did the moisture content in the top 0-40 cm for maize and 0-60 cm for sunflower
 597 decrease below the moisture content at -33kPa. During the growing season, the
 598 variation of moisture content was greater in the top 60 cm with the majority of the
 599 roots than in the lower depths where, after the first irrigation, it remained nearly
 600 constant close to saturation.



601

602 Fig. 5 Observed (blue dots) and simulated soil moisture content of the Shahaoku
 603 experimental fields during model calibration (a,b,c) and validation (d,e,f)



604
 605 Fig. 6 Observed (blue dots) and simulated soil salinity concentration of the
 606 experimental fields in Shahaoku during model calibration (a,b,c) and validation (d,e,f).

607 4.1.4 Salinity

608 Overall the salt concentration is greatest at the surface and increases at all
 609 depths during the growing season. Sunflower is more salt tolerant than maize and the
 610 overall salt concentration was greater in the sunflower fields (Fig. 6) at comparable
 611 times of the crop development for field B but not for field C. Comparing the salt
 612 concentration and soil moisture patterns (Fig.5), we note that they behave similarly

613 but opposite to each other (Fig. 6). The soil salinity concentration was decreasing
614 during an irrigation event due to dilution and then gradually increasing partly due to
615 evaporation of the water. Some of the soil salt was transported to the layers below
616 during irrigation and some salt was moving upward with the evaporation from the
617 surface. As expected, after the harvest, the autumn irrigation decreased the salt
618 concentration from fall 2017 to spring 2018.

619 4.1.5 Groundwater observations

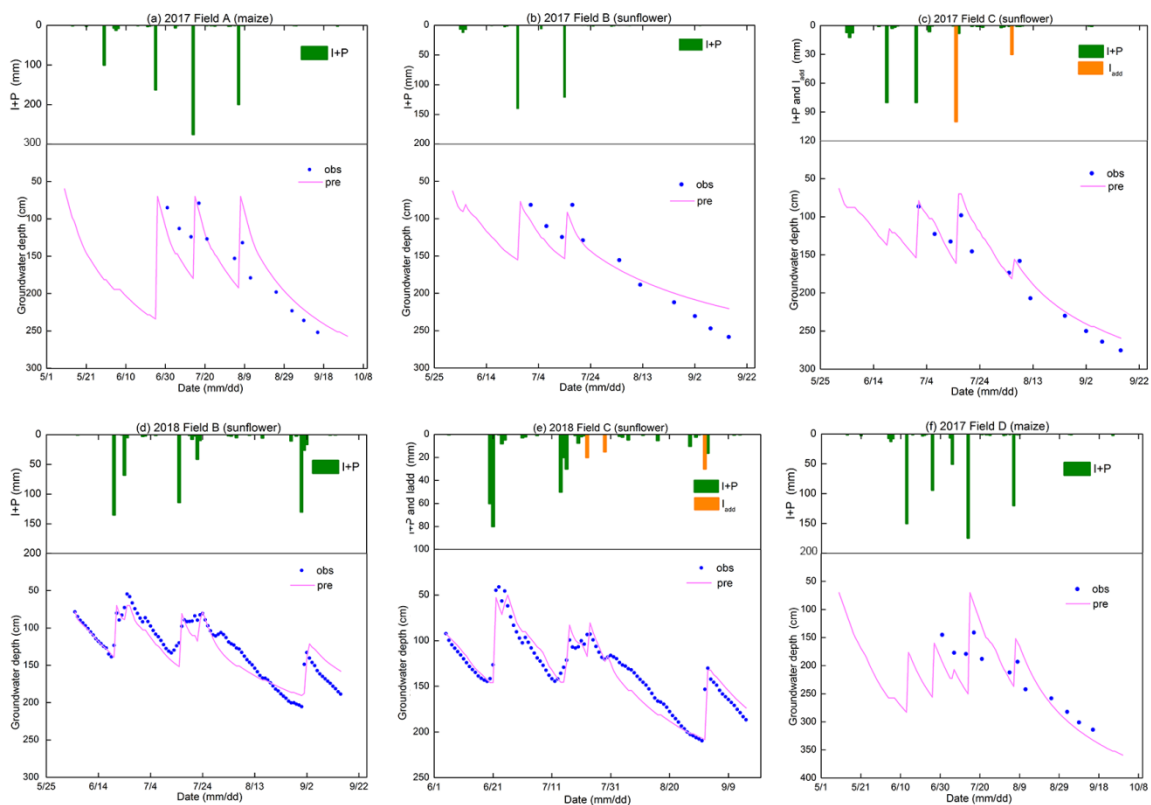
620 The variation in groundwater depth during the growing season was very similar
621 for both years and in all fields. The groundwater depth for all fields was between 50
622 and 100 cm from the surface after an irrigation event and then decreased to around
623 150 cm before the next irrigation or rainfall (Fig.7). Only after the last irrigation in
624 August 2017 did the water table decrease to below 250 cm and to around 200 cm in
625 2018. Field D followed the same pattern but the groundwater was more down from
626 the surface. In several instances, the groundwater table increased without an
627 irrigation or rainfall event in sunflower field C (Fig. 7c and 7e). This was likely related
628 to an irrigation event either from an irrigation in nearby field that affected the overall
629 water table or an accidental irrigation that was not properly documented. We
630 estimated the amount of irrigation water based on the change in moisture content in
631 the soil profile (orange bars in Fig. 7c and 7e). Finally, there was a notable rise in the
632 water table of an mean 375mm “autumn irrigation” after harvest between the end of
633 2017 (Figs. 7 a, b, c) and the beginning of 2018 (Figs. 7 d, e, f), which is a common
634 practice in the Jiefangzha irrigation district to leach the salt that has accumulated in

635 the profile during the growing periods.

636 Note that in Fig. 7, after an irrigation event, the groundwater depth was between
637 50-80 cm while the whole profile was saturated (Fig. 5). This is directly related to the
638 bubbling pressure of the water. After the irrigation event stopped, the water table was
639 likely at the surface but then immediately decreased because a small amount of
640 evaporated water will bring the water table down to a depth of approximately equal to
641 the bubbling pressure, φ_b , in Eq. 5. The bubbling pressures are listed in Table 3.

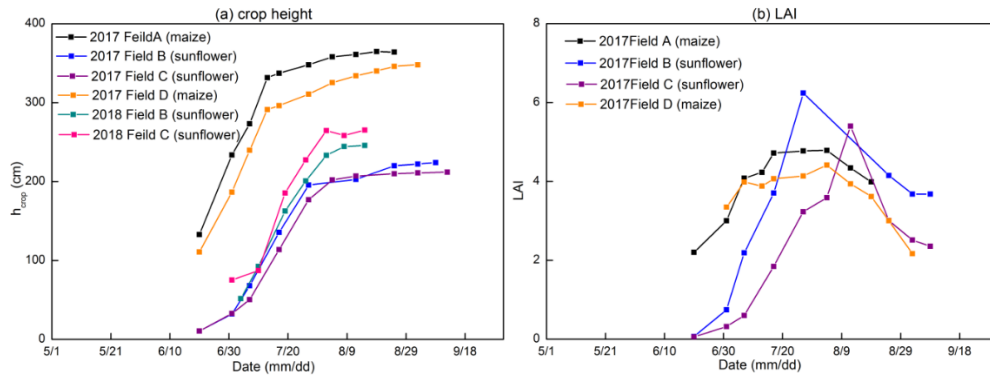
642 4.1.6 LAI and plant height

643 Plant height and LAI followed the typical growth curve that started slowly to rise
644 in the beginning, accelerated during the vegetative stage and then became constant
645 during the seed setting and ripening stages (Fig. 8). In the maturing stage, the leaf
646 area index decreased.



647

648 Fig. 7. Observed (blue dots) and simulated groundwater depth of the experimental
649 fields in Shahaoqu during model calibration (a, b, c) and validation (d, e, f)



650

651 Fig. 8 Observed crop height (a) and leaf area index (b) of the experimental field in
652 Shahaoqu in 2017 and 2018.

653

654 4.2 Soil Characteristic curve and drainable porosity

655 To simulate the soil moisture content and to derive drainable porosity as a function of
656 water table depth, the soil moisture characteristic curves were derived by plotting the
657 observed soil moisture content in 2017 and 2018 versus the height above the water
658 table to the soil surface for the five soil layers in Fig. 9. The Brooks-Corey equation
659 (Brooks and Corey, 1964) was fitted through outer envelope of the points. The
660 parameters of the Brooks-Corey equation were adjusted through a trial and error to
661 obtain the best fit (Table 3a). In Fig. 9, points on the left side of the soil moisture
662 characteristic curve (moisture content smaller than the field capacity) were due to
663 water removal at times when evaporative demand was greater than the upward water
664 flux. Under these conditions the conductivity is limiting in the soil and there is no
665 relationship between groundwater depth and matric potential. Since we take the
666 water table depth as proxy for matric potential, these points are omitted when drawing
667 the soil characteristic curve. The few points at the right of the soil moisture

668 characteristic curve indicate the soil moisture was greater than field capacity and
 669 matric potential and groundwater were not yet at equilibrium after an irrigation event.

670 The fitted parameter values are consistent. Field A had a greater bubbling
 671 pressure and moisture content at -33 kPa than the other fields indicating that this field
 672 had more clay. This was confirmed by the data in Table 2. For fields B, C and D, the
 673 bubbling pressure was greater at the 60-80 cm depth or the 80 -100 cm depth, which
 674 was also in accordance with the data in Table 2.

675 Table 3a Calibrated soil hydraulic parameters in the Brooks and Corey soil moisture
 676 characteristic curve.

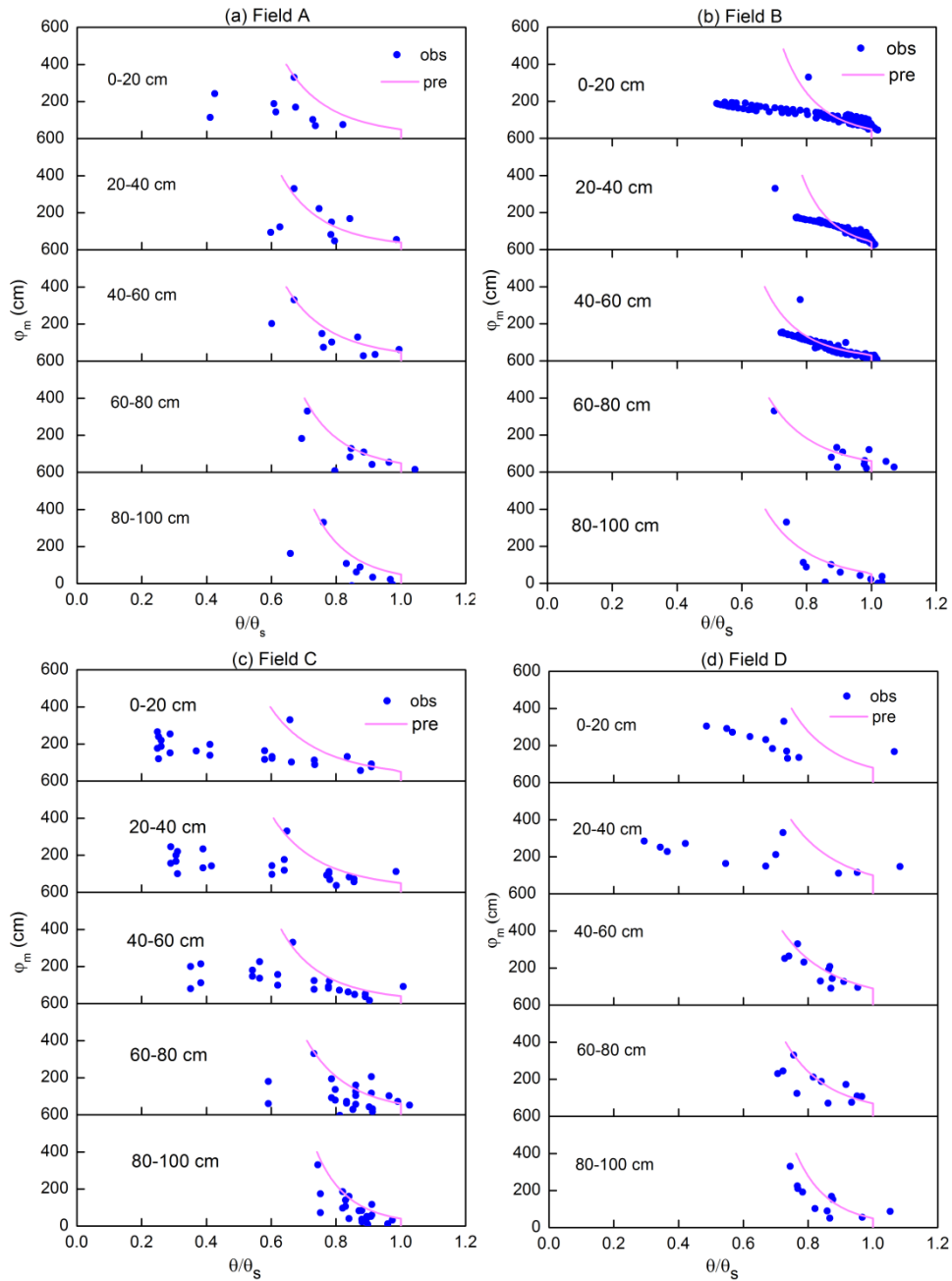
Field	Parameter	0-20cm	20-40cm	40-60cm	60-80cm	80-100cm
A	θ_s	0.4	0.36	0.43	0.45	0.47
	φ_b	80	100	90	70	50
	λ	0.18	0.21	0.22	0.18	0.15
B	θ_s	0.35	0.37	0.41	0.4	0.4
	φ_b	50	55	33	60	55
	λ	0.14	0.11	0.16	0.2	0.2
C	θ_s	0.38	0.37	0.39	0.71	0.43
	φ_b	55	50	40	60	40
	λ	0.26	0.24	0.2	0.18	0.13
D	θ_s	0.4	0.36	0.45	0.45	0.44
	φ_b	50	40	55	50	50
	λ	0.21	0.2	0.3	0.17	0.15

677 Note: θ_s is the soil moisture at saturation ($\text{cm}^3\text{cm}^{-3}$), φ_b is bubbling pressure (cm), λ is
 678 the pore size distribution index.

679 Table 3b Calibrated groundwater parameters

Field\parameters	A	B	C	D
a	70	75	110	70
b	0.02	0.025	0.022	0.015

680



681

682 Figure. 9 Soil moisture characteristic curves of five soil layers in the experimental
 683 fields. The pink line is the fit with the Brooks-Corey equation.

684

685 4.3 Parameters sensitivity analysis

686 The results of sensitivity analysis of the 15 input parameters on 5 output parameters

687 are shown in Fig. 10. The evaluated output parameters are soil moisture content,

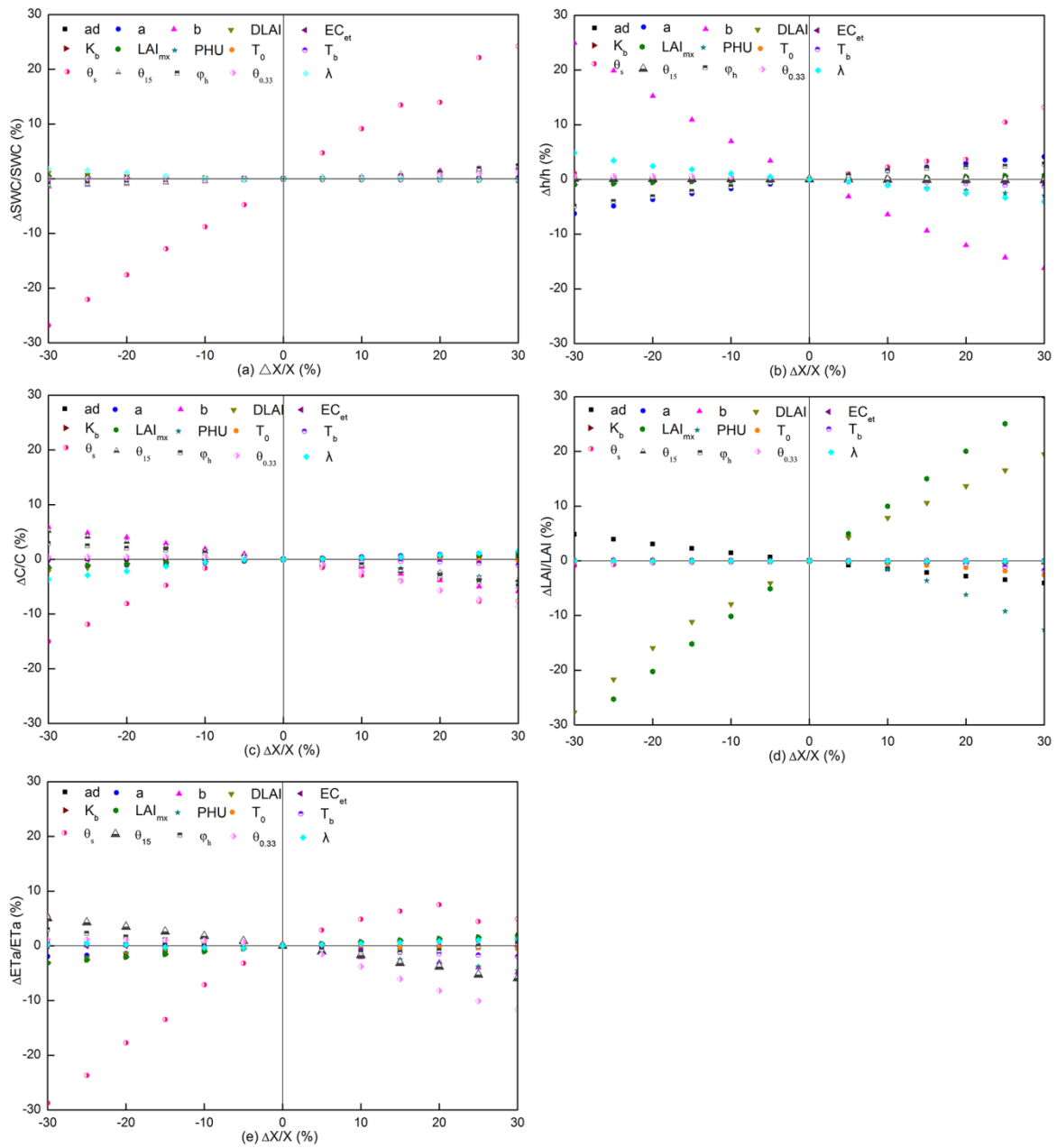
688 groundwater depth, soil salinity concentration, field evapotranspiration, and crop leaf

689 area index (LAI). Steeper lines indicate a greater sensitivity of the parameter.

690 The results of the sensitivity analysis show that moisture content predictions (Fig
691 10a) are the most sensitive to the input value of the saturated moisture content (θ_s).
692 None of the other parameters are very sensitive. This includes the shape parameters
693 for the soil characteristic curve, bubbling pressure φ_b , and the exponent λ . The input
694 parameter with the most sensitivity for *groundwater depth* (Fig. 10b), is the saturated
695 moisture content as well. Other less sensitive parameters are the exponent b and
696 constant a in Eq. 23 in predicting the upward flux and the bubbling pressure, φ_b , of the
697 soil moisture characteristic curve (Eq. 8a). Likewise, in case of the *salinity* predictions
698 (Fig. 10c), the saturated moisture content gives the greatest relative change in salt
699 content. Less sensitive, but still important, are the field capacity, θ_{fc} , the bubbling
700 pressure, φ_b , and the exponent λ of the soil characteristic curve (Eq. 8a) and b in Eq.
701 23. The sensitive parameters for the *leaf area index (LAI)* (Fig 10d) are the maximum
702 potential leaf area index, LAI_{mx} , and fraction of growing season when leaf area
703 declines (*DLAI*) followed by total potential heat units required for crop maturation
704 (*PHU*). Finally, for the *evapotranspiration* (Fig 10e), the saturated soil moisture
705 content is the most sensitive parameter, and other less sensitive parameters are the
706 exponent b and field capacity.

707 Thus, the model output is most sensitive to the input parameters that define the
708 soil hydraulic properties, groundwater flux and crop growth. As expected, since the
709 soil remains near field capacity, the parameters that relate to the reduction of
710 evaporation when the soil dries out are insensitive. When used in the simulation

711 practices, the model needs to be calibrated and verified to avoid high error from
 712 parameters uncertainty.



713
 714 Figure. 10 Parameters sensitivity analysis for (a) soil moisture content, (b)
 715 groundwater depth, (c) salt salinity concentration, (d) LAI, (e) ET
 716

717 4.4 Model calibration and validation with field data

718 The model parameters were calibrated and validated using the observed moisture

719 contents, groundwater depth, plant height, leaf area index and the calculated
720 evapotranspiration. For calibration, the data collected in 2017 were used for
721 sunflower fields B and C and maize field A. Since farmers did not grow maize in 2018,
722 the 2017 data of maize field D, together with sunflower fields B and C in 2018 were
723 used for validation. The optimal parameter set was determined using graphical
724 similarity between observed and predicted results together with near optimum
725 performance of the statistical indicators while keeping all values within physical
726 acceptable ranges.

727 As a way of reducing the number of parameters that needed to be calibrated, we
728 initially selected one to three most sensitive parameters for each of the observed time
729 series, starting with evapotranspiration (including LAI and crop height) followed by
730 moisture content, groundwater depth, and salt content in the soil. This cycle was
731 repeated several times until changes became small. The last stage of the calibration
732 consisted of fine-tuning the remaining least sensitive parameters.

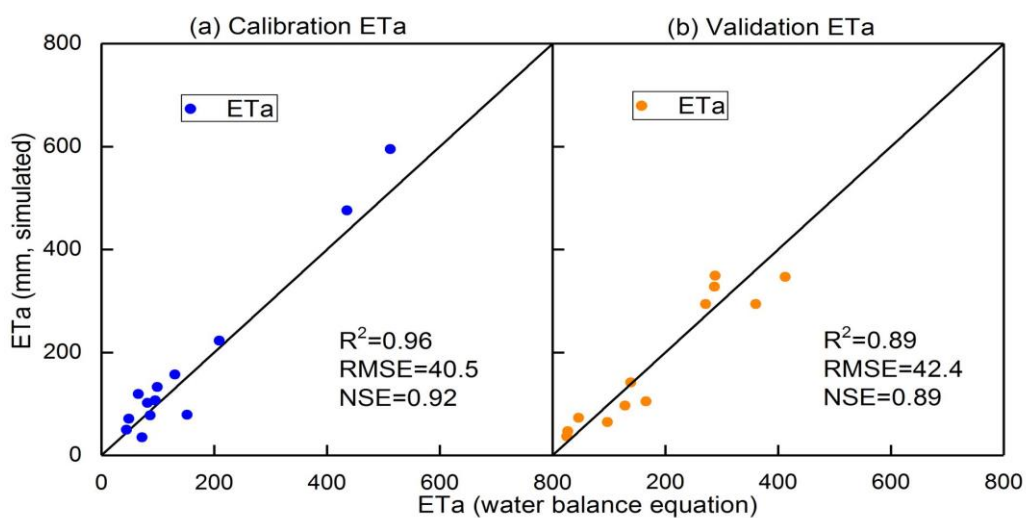
733 To calibrate the parameters in the CROP module, we calculated
734 evapotranspiration during the crop growth period with the observed soil moisture
735 content and groundwater depth by the soil water balance method. In addition, we
736 used the observed LAI measurements in 2017 and plant height in both 2017 and
737 2018. LAI was not measured in 2018. The $DLAI$, LAI_{mx} and H_{mx} in the crop module
738 were adjusted to fit the observed LAI and crop height values. In addition, we fitted the
739 θ_{fc} moisture content to obtain a good fit of the evapotranspiration. The saturated
740 moisture content values were not adjusted since they were already determined for

741 fitting the soil characteristic curve. The exponent b and constant a in Eq. 23 were
742 adjusted to fit the observed soil moisture content and groundwater depth.

743

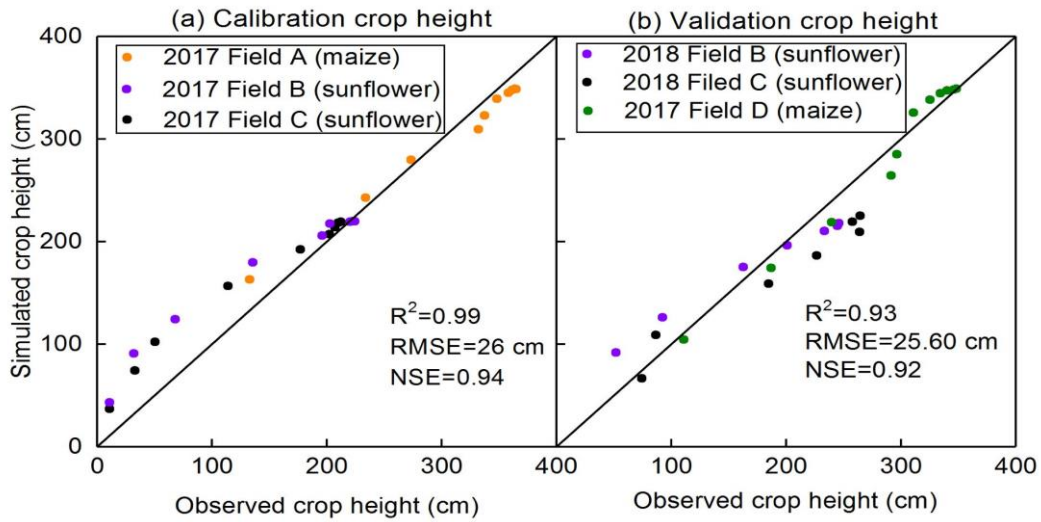
744 4.4.1 Evapotranspiration, crop height and leaf area index

745 The predicted evapotranspiration and that calculated from the mass balance
746 show a good agreement with Nash Sutcliff values ranging from 0.96-0.89 during
747 calibration and validation (Fig. 11 and Table 4). The calibrated predictions of plant
748 height fitted the observed values well during calibration and validation with Nash
749 Sutcliff values ranging from 0.77-0.96 for the individual fields (Table 4) and over 90%
750 when the data was pooled for the fields during calibration and validation (Fig.12). LAI
751 was not measured in 2018. During calibration, Nash Sutcliff predicted LAI values
752 were good for sunflower but not as good for maize but the coefficient of determination
753 and slope in the regression were acceptable (Table 4, Fig. 13). In addition, the overall
754 trend was predicted reasonably well (Fig. 13b).



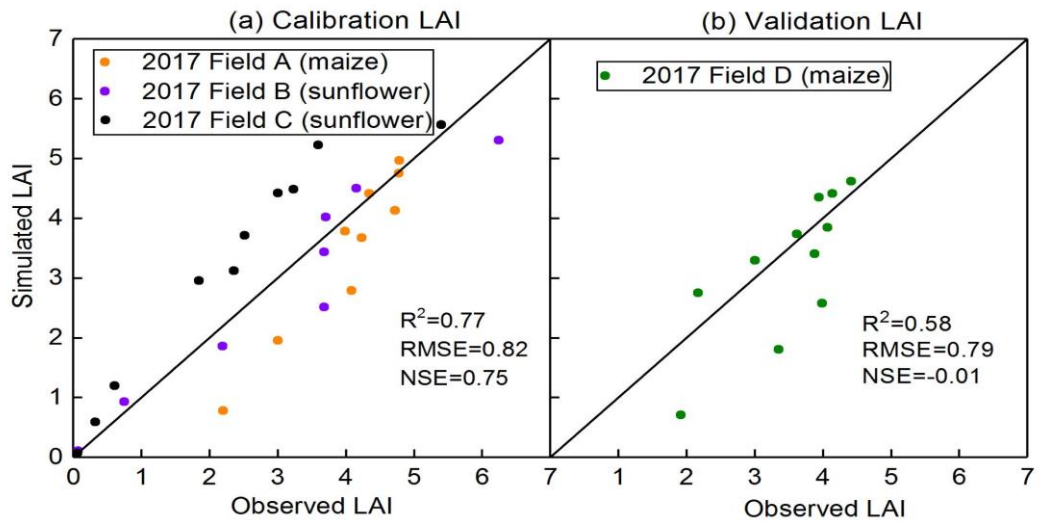
755

756 Fig. 11 Comparison of predicted and observed actual evapotranspiration: a)
757 Calibration and b) Validation



758
759
760
761

Fig.12 Comparison of predicted and observed crop height: a) Calibration and b) Validation



762
763
764
765
766
767
768
769

Fig. 13 Comparison of predicted and observed LAI: a) Calibration and b) validation

770 Table 4 Model error statistics for calibration and validation of model in 2017 and 2018
 771 (Mean relative error, MRE; root mean square error, RMSE; Regression slope;
 772 Coefficient of determination, R²; Regression coefficient, slope).

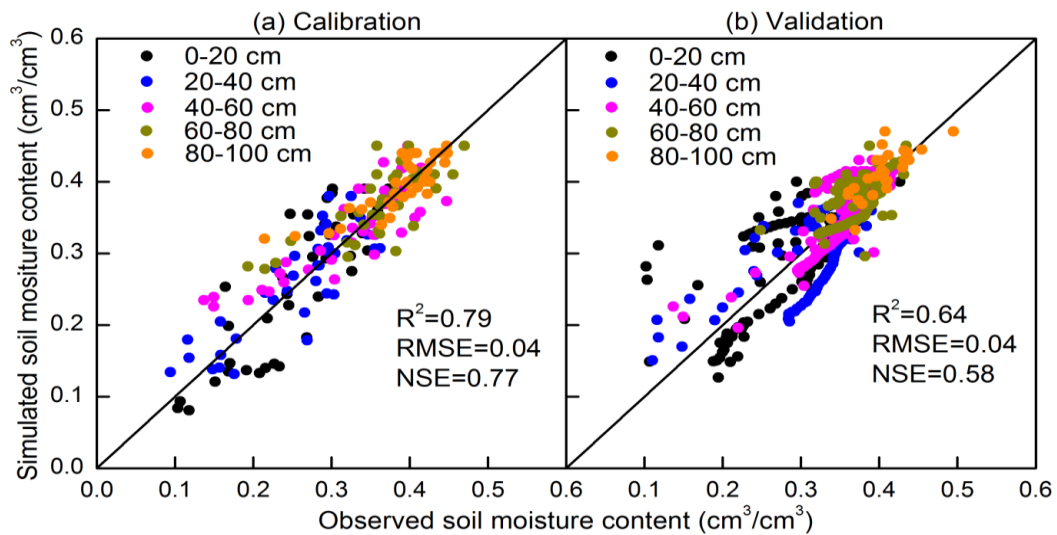
Process	Field	Variable	MRE (%)	RMSE (cm ³ cm ⁻³ cm or gL ⁻¹ or mm)	NSE	R ²	Regression coefficient slope
Calibration	2017 Field A (maize)	SWC (0-1m)	2.9	0.04	0.8	0.56	1.01
		GWD	4.5	33.8	0.64	0.64	0.97
		LAI	-17.4	0.78	0.11	0.92	0.89
		hcrop	0.04	16.2	0.95	0.99	0.97
		C (0-1m)	13.9	0.5	*	0.49	1.07
	2017 Field B (sunflower)	SWC (0-1m)	-1.2	0.04	0.71	0.74	0.97
		GWD	6.0	22.9	0.86	0.98	0.96
		LAI	4.7	0.58	0.9	0.92	0.91
		hcrop	6.8	33.5	0.83	0.96	1.1
		C (0-1m)	11.0	0.55	*	0.7	1.1
	2017 Field C (sunflower)	SWC (0-1m)	8.5	0.04	0.88	0.9	1.05
		GWD	-7.3	19.1	0.91	0.94	0.94
		LAI	48.6	1.0	0.59	0.93	1.29
		hcrop	5.42	27.4	0.88	0.98	1.07
		C (0-1m)	-1.6	0.52	*	0.08	0.94
Validation	2018 Field B (sunflower)	ETa	12.2	40.5	0.92	0.96	1.11
		SWC (0-1m)	-2.3	0.03	0.43	0.68	0.98
		GWD	4.86	16.1	0.83	0.84	1.01
		hcrop	12.5	26.9	0.86	0.99	0.95
	2018 Field C (sunflower)	C (0-1m)	4.0	0.35	*	0.72	1.06
		SWC (0-1m)	17.3	0.06	0.64	0.72	1.04
		GWD	2.1	13.8	0.86	0.87	1.01
		hcrop	-10.3	36.4	0.77	0.97	0.84
	2017 Field D (maize)	C (0-1m)	0.51	0.33	*	0.73	1.02
		SWC (0-1m)	6.1	0.04	0.68	0.77	1.05
		GWD	0.64	39.1	0.52	0.71	1.01
		LAI	-10.7	0.79	-0.02	0.58	0.93
		hcrop	-1.7	13.6	0.96	0.98	1
		C (0-1m)	9.8	0.51	*	0.54	1.11
		ETa	8.0	42.4	0.89	0.89	0.95

773 Note: * Relative bias was over 5% invalidating the calculation of NSE. SWC is the soil
 774 moisture content, GWD is the groundwater depth, LAI is the leaf area index, hcrop is
 775 the height of the crop, C is the soil salinity concentration, ETa is the actual
 776 evapotranspiration.

777 *4.4.2 Soil moisture and groundwater depth*

778 Next, the moisture contents and groundwater table were fitted with the parameters in
779 the Vadose model without changing the parameters in the CROP module. Saturated
780 moisture content was the most sensitive parameter for calibrating the moisture
781 content (Fig.10a). Since this value was already determined a priori from the soil
782 characteristic curve (Table 3a), we could not use other parameters to obtain a better
783 fit since none were sensitive (Fig.10a). Therefore, we calibrated the groundwater
784 parameters (i.e., a and b parameters (Eq. 23)) together with the moisture content to
785 obtain the best fit for both. The fitted a and b values are listed in Table 3b. The fitted
786 parameters between the four experimental fields were similar but not the same. This
787 can be expected in river plains where soils can vary over short distances.

788 Overall, the moisture contents were predicted well during calibration and
789 validation (Figs. 5, 14 and Table 4) with the exception of field B during validation
790 (Table 4) with a NSE of 0.43. The moisture contents were predicted most accurately
791 in the layers from 40-100cm where the soil moistures were at field capacity during
792 most of the growing season (Fig. 14). In the top 40 cm, the predicted soil moisture
793 content deviated from observed moisture contents, especially at the dryer end (Fig. 5
794 and 14). Unlike at deeper depths, evapotranspiration determined the moisture
795 contents at shallow depths. Prediction of evapotranspiration introduced additional
796 uncertainties such as the distribution of the root system. This uncertainty is also likely
797 the reason why the 2018 moisture contents during the validation are acceptable but
798 not predicted as well as in 2017.

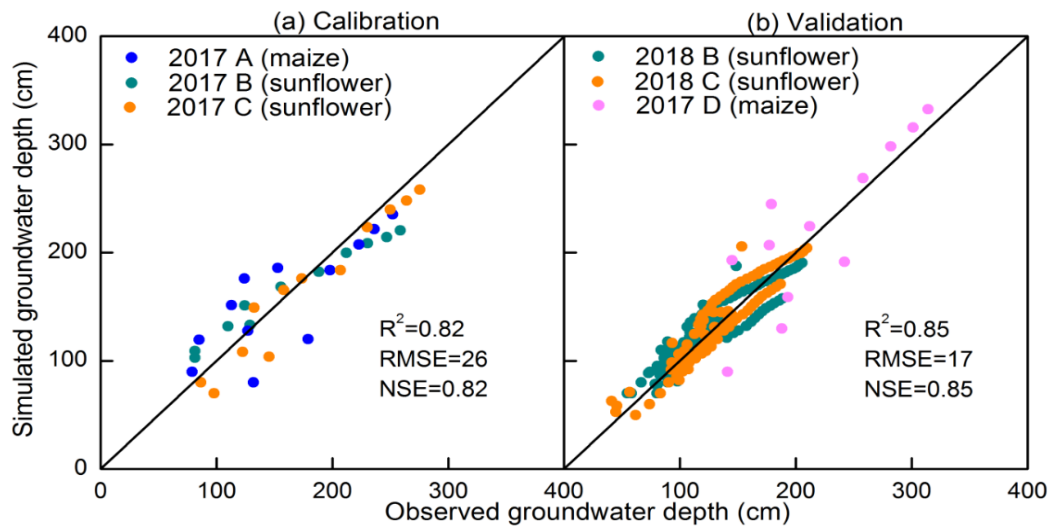


799

800 Fig. 14 Comparison of predicted and observed soil moisture content: a) calibration
 801 and b) validation

802

803 The predicted and observed groundwater depths are in good agreement during
 804 both calibration and validation (Figs 7, 15). The MRE values were within $\pm 10\%$ and
 805 the NSE values ranged from 0.52 for field D during validation to 0.91 in field C during
 806 calibration where some of the recharge events were estimated (Table 4).

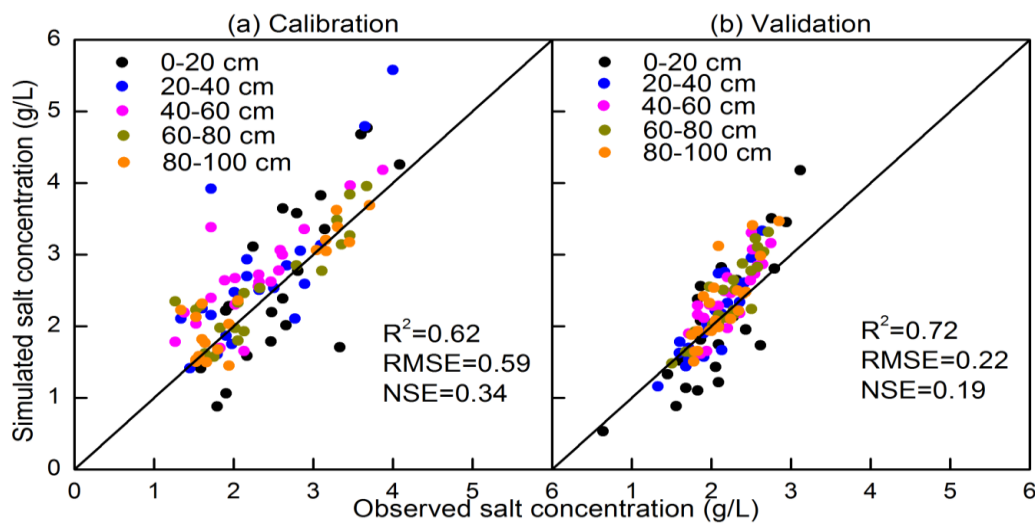


807

808 Fig. 15 Comparison of predicted and observed groundwater depth a) calibration and
 809 b) validation.

810 4.4.3 Soil salinity

811 The only parameter that could be adjusted each year for calibration of the salt
 812 concentrations was the initial salt concentration. The predicted salt concentrations in
 813 the top layers decreased after an irrigation event similar to the limited observed values
 814 (Figs. 6). Despite that the salt concentration fitted visually reasonably well as shown in
 815 Figures 6 and 16, there was a bias of 8% in the data and consequently the Nash
 816 Sutcliff efficiency could not be applied (Table 4) (Ritter and Muñoz-Carpena, 2013).
 817 Similarly to the moisture contents, the salt concentrations in the layers below 40 cm
 818 were predicted more accurately than the layers above the 40 cm. More data should be
 819 collected during the whole year on the salt concentrations in the soil in order to
 820 accurately predict the salt concentrations.



821
 822 Fig. 16 Comparison of predicted and observed salt concentration during calibration (a)
 823 and validation (b)

824 **5. Discussion**

825 The EPICS model is a surrogate model that can be applied in areas with shallow
 826 groundwater. It can simulate the soil moisture content and salt concentration for
 827 layers in the soil, the groundwater depth, upward movement of water from

828 groundwater, evapotranspiration, and plant growth.

829 The model is different from traditional models that are based on Richards
830 equation; instead of calculating the fluxes first, in the EPICS model, the groundwater
831 depth is calculated first based either on the amount of water removed by
832 evapotranspiration on days without rain or irrigation or recharge to groundwater on
833 the other days. Subsequently, when the groundwater is sufficiently shallow and the
834 potential upward flux from the groundwater is greater than the evaporative demand,
835 the moisture contents are adjusted so that soil moisture and groundwater depth are in
836 equilibrium (i.e., field capacity). In this case, the matric potential is equal to the height
837 above the water table and the moisture contents can be found with the soil
838 characteristic curve. When the upward flux is less than the evaporative demand of the
839 atmosphere and crop, the difference between the upward moisture content is
840 determined by first decreasing the moisture content below the field capacity. The flux
841 of water in the soil is then calculated based on the changes in water content. The
842 advantage is fewer input parameters needed when compared with other numerical
843 models (Šimůnek et al., 1996; Dam et al., 1997). For example, the hydraulic
844 conductivity is not used in EPICS.

845 Although the uncertainties of field experimental observations and input data of
846 the model affected the accuracy of simulation results, EPICS compares well with
847 other models. Xu et al. (2015) tested the SWAP-EPIC for two lysimeters grown with
848 maize on the same experimental farm in the Hetao irrigation district where our
849 experiment was carried out. The SWAP model solves the Richards' Equation

850 numerically with an implicit backward scheme and is combined by Xu et al. (2015)
851 with the EPIC model. The accuracy of our simulation results, despite the difference in
852 complexity, are very similar. The moisture contents were simulated slightly better with
853 EPICS, the groundwater depth was nearly the same, and the LAI values were
854 predicted more accurately in the SWAP-EPIC model. Xue et al. (2015) did not
855 simulate the salt content of the soil. Compared to less data and computational
856 intensive models that are applied in the Yellow River, the soil moisture content were
857 simulated more accurately by EPICS than in the North China Plain with 30 m deep
858 groundwater by surrogate models of Kendy et al. (2003) and Yang et al. (2015 a,b)
859 and in the Hetao irrigation district by Gao et al. (2017b) and Xue et al. (2018) during
860 the crop growth period.

861 To obtain more accurate results in the future, the upward capillary flux from
862 groundwater needs to be improved. Also, future refinement of the model would be
863 served by measuring the salinity of irrigation source water. This would be more
864 important if this model was implemented for irrigation that depends on groundwater
865 sources, especially hydrologically closed basins. In addition, the evapotranspiration
866 measured independently, using Eddy covariance (Zhang et al., 2012; Armstrong et al.,
867 2008) and Bowen ratio-energy balance method (Zhang et al., 2007) should be further
868 used to test performance of the model in the future study.

869 The limitation of the EPICS model is it can only be applied in areas where
870 groundwater is generally less than 3.3 m deep. When the groundwater is deeper than
871 3.3 m, the field capacity of the surface soil is determined by the moisture content

872 when the hydraulic conductivity becomes limiting and not by the depth of the
873 groundwater.

874 Overall, the present model has the advantage that it greatly simplifies the
875 calculation of the moisture content, groundwater depth and salt content and despite
876 that, gives results similar to or better than other models applied in the Yellow river
877 basin.

878 **6. Conclusions**

879 A novel surrogate field hydrological model called *Evaluation of the Performance*
880 *of Irrigated Crops and Soils* (EPICS) was developed for irrigated areas with shallow
881 groundwater. The model was tested with two years experimental data collected by us
882 for sunflower and one year of maize on replicated fields in the Hetao irrigation district,
883 a typical arid to semi-arid irrigation district with a shallow aquifer. The EPICS model
884 uses the soil moisture characteristic curve, upward capillary flux, and groundwater
885 depth to derive the drainable porosity and predict the soil moisture contents and
886 salinity. The evaporative flux is calculated with equations in EPIC (Environmental
887 Policy Integrated Climate) and root distribution equation.

888 The simulation results show that the EPICS model can predict the soil moisture
889 content and salt concentration in different soil layers, groundwater depth, and crop
890 growth on a daily time step with acceptable accuracy during calibration and validation.
891 The saturated soil moisture content is the most sensitive parameter for soil moisture
892 content, salt concentration, and ET in our model.

893 In the future, the model should be tested in other areas with shallow groundwater

894 that can be found in surface irrigated sites and in humid climates in river plains. Once
895 fully tested, the EPICS model can be used for optimizing water use at the local scale
896 but, more importantly, on a watershed scale in closed basins where every drop of
897 water counts.

898

899 **Data availability:** The observed data used in this study are not publicly accessible.
900 These data have been collected by personnel of the College of Water Resources and
901 Civil Engineering, China Agricultural University, with funds from various cooperative
902 sources. Anyone who would like to use these data, should contact Zhongyi Liu,
903 Xianghao Wang and Zailin Huo to obtain permission.

904 **Author contributions:** LZ and XW collected the data. ZL, ZH, CW, GH, XX and TS
905 contributed to the development of the model. The simulations with the model were
906 done by ZL, ZH and TS. Preparation and revision of the paper were done by ZL under
907 the supervision of TS and ZH.

908 **Competing interests:** The authors declare that they have no conflicts of interest.

909 **Acknowledgements:** Peggy Stevens helped greatly with polishing the English. We
910 thank Xianghao Wang and Limin Zhang and the technicians in the Shahaoqu
911 experimental station who helped in collecting data.

912 **Financial support:** This study has been supported by National Key Research and
913 Development Program of China (2017YFC0403301) and the National Natural
914 Science Foundation of China (No. 51639009, 51679236).

915

916

917

918

919

References

920 Abrahart, R.J and See, L.: Comparing neural network and autoregressive moving
921 average techniques for the provision of continuous river flow forecasts in two
922 contrasting catchments. *Hydro. Processes*, 14: 2157-2172. [http://doi.org/10.1002/1099-1085\(20000815/30\)14:11/12<2157::AID-HYP57>3.0.CO;2](http://doi.org/10.1002/1099-1085(20000815/30)14:11/12<2157::AID-HYP57>3.0.CO;2-S)
923 -S. 2000.

925 Allen, R.G., Pereira, L.S., Raes, D., and Smith, M.: Crop evapotranspiration.
926 Guidelines for computing crop water requirements-FAO Irrigation and Drainage
927 Paper 56, FAO, Rome. 1998

928 Armstrong, R.N., Pomeroy, J. W., Martz, L.W.: Evaluation of three evaporation
929 estimation methods in a Canadian prairie landscape. *Hydrol. Process*, 22(5):
930 2801-2815. <https://doi.org/10.1002/hyp.7054>. 2008.

931 Asher, M.J., Croke, B.F.W., Jakeman, A.J. and Peeters, L.J.M.: A review of surrogate
932 models and their application to groundwater modeling. *Water Resour Res*,
933 51:5957-5973. <http://doi.wiley.com/10.1002/2015WR016967>. 2015. Blanning, R.
934 W., The construction and implementation of metamodels, *Simulation*, 24(6):
935 177-184. <https://doi.org/10.1177/003754977502400606>. 1975.

936 Babajimopoulos, C., Panoras, A., Georgoussis, H., Arampatzis, G., Hatzigiannakis, E.,
937 Papamichail, D.: Contribution to irrigation from shallow water table under field
938 conditions. *Agr. Water Manage.* 92:2015-210. <https://doi.org/10.1016/j.agwat.2007.05.009>

940

941 Brooks, R.H., and Corey, A.T.: Hydraulic properties of porous media, *Hydrology*
942 Paper 3. Colorado State University. Fort Collins, Colorado, 37pp, 1964.

943 Blanning, R.W.: Construction and Implementation of Metamodels. *Simulation*,
944 24(6):177-184. <https://doi.org/10.1177/003754977502400606>. 1975.

945 Chen, C., Wang, E., and Yu, Q.: Modelling the effects of climate variability and water
946 management on crop water productivity and water balance in the North China

947 Plain. Agr. Water Manage., 97:1175-1184. [https://](https://doi.org/10.1016/j.agwat.2008.11.012)
948 doi.org/10.1016/j.agwat.2008.11.012. 2010.

949 Chen, S., Huo, Z., Xu, X., Huang, G.: A conceptual agricultural water productivity
950 model considering under field capacity soil water redistribution applicable for arid
951 and semi-arid areas with deep groundwater, *Agr Water Manage*, 213, 309-323.
952 [https:// doi.org/10.1016/j.agwat.2018.10.024](https://doi.org/10.1016/j.agwat.2018.10.024). 2019.

953 Cloke, H., Pappenberger, F., Renaud, J.: Multi-Method Global Sensitivity Analysis
954 (MMGSA) for modelling floodplain hydrological processes. *Hydrol Process*, 22(1):
955 1660-1674. [https:// doi.org/ 10.1002/hyp.6734](https://doi.org/10.1002/hyp.6734). 2008.

956 Cuo, L., Giambelluca, T., Ziegler, A.: Lumped parameter sensitivity analysis of a
957 distributed hydrological model within tropical and temperate catchments. *Hydrol*
958 *Process*, 25(15): 2405-2421. [http://doi.org/ 10.1002/hyp.8017](http://doi.org/10.1002/hyp.8017). 2011.

959 Dam, JC. Van., Huygen, J, Wesseling, JG, Feddes, RA., Kabat, P.,Walsum, PEV.
960 Van.,Groenendijk, P., Diepen.: Theory of SWAP version 2.0. Simulation of water
961 flow, solute transport and plant growth in the soil-water-atmosphere-plant
962 environment. Report 71, Department Water Resources, Wageningen Agricultural
963 University. Technical document 45, DLO Winand Staring Centre,
964 Wageningen,152pp, 1997.

965 Dawson, C.W., Abrahart, R.J., Shamseldin, A.Y., Wilby, R.L.: Flood estimation at
966 ungauged sites using artificial neural networks. *J Hydrol*.319: 391-409.
967 [http://doi.org/10.1016/ .jhydrol.2005.07.032](http://doi.org/10.1016/j.jhydrol.2005.07.032). 2006.

968 Dehaan, R., and Taylor, G.: Field-derived spectra of salinized soils and vegetation as
969 indicators of irrigation-induced soil salinization, *Remote Sens Environ*, 80(3),
970 406-417. [https:// doi.org/10.1016/S0034-4257\(01\)00321-2](https://doi.org/10.1016/S0034-4257(01)00321-2). 2002.

971 Delonge, K. C., Ascough, J. C., Andales, A. A., Hansen, N. C., Garcia, L. A., Arabi, M.:
972 Improving evapotranspiration simulations in the CERES-Maize model under
973 limited irrigation. *Agr Water Manage*, 115: 92-103. [http://doi.org/](http://doi.org/10.1016/j.agwat.2012.08.013)
974 [10.1016/j.agwat.2012.08.013](http://doi.org/10.1016/j.agwat.2012.08.013). 2012.

975 Doherty, J. and Simmons C.: Groundwater modelling in decision support: reflections
976 on a unified conceptual framework, *Hydrogeol. J*, 21(7), 1531-1537. [https://](https://doi.org/10.1007/s10040-013-1027-7)
977 doi.org/10.1007/s10040-013-1027-7. 2013.

- 978 Feng, Z., Wang, X., Feng, Z.: Soil N and salinity leaching after the autumn irrigation
979 and its impact on groundwater in Hetao Irrigation District, China. *Agr Water*
980 *Manage*, 71(2): 131-143. [https:// doi.org/10.1016/j.agwat.2004.07.001](https://doi.org/10.1016/j.agwat.2004.07.001). 2005.
- 981 Flint, A.L., Flint, L.E., Kwicklis, E.M., Fabryka-Martin, J.T., and Bodvarsson, G.S.:
982 Estimating recharge at Yucca Mountain, Nevada, USA: comparison of methods.
983 *Hydrogeol. J.*, 10:180-204. [https:// doi.org/ 10.1007/s10040-001-0169-1](https://doi.org/10.1007/s10040-001-0169-1). 2002.
- 984 Gao, X., Huo, Z., Bai, Y., Feng, S., Huang, G., Shi, H., and Qu, Z.: Soil salt and
985 groundwater change in flood irrigation field and uncultivated land: a case study
986 based on 4-year field observations. *Environ. Earth Sci.*, 73:2127-2139. [https://](https://doi.org/10.1007/s12665-014-3563-4)
987 doi.org/10.1007/s12665-014-3563-4. 2015.
- 988 Gao, X., Huo, Z., Qu, Z., Xu, X., Huang, G., and Steenhuis, T.S.: Modeling
989 contribution of shallow groundwater to evapotranspiration and yield of maize in
990 an arid area. *Sci. Rep-UK* 7. [https:// doi.org/10.1038/srep43122](https://doi.org/10.1038/srep43122). 2017.
- 991 Gardner, W.: Some steady-state solutions of the unsaturated moisture flow equation
992 with application to evaporation from a water table. *Soil Sci.*, 85:228-232. 1958.
- 993 Gardner, W., Hillel, D., and Benyamini, Y.: Post-Irrigation Movement Soil Water 1.
994 Redistribution. *Water Resour Res.*, 6:851-860. [https:// doi.org/](https://doi.org/10.1029/WR006i003p00851)
995 [10.1029/WR006i003p00851](https://doi.org/10.1029/WR006i003p00851). 1970a.
- 996 Gardner, W., Hillel, D., and Benyamini, Y.: Post-Irrigation Movement of Soil Water 2.
997 Simultaneous Redistribution and Evaporation. *Water Resour Res.*, 6:1148-1153.
998 [https:// doi.org/ 10.1029/WR006i004p01148](https://doi.org/10.1029/WR006i004p01148). 1970b.
- 999 Guo, S., Ruan, B., Chen, H., Guan, X., Wang, S., Xu, N. and Li, Y.: Characterizing the
1000 spatiotemporal evolution of soil salinization in Hetao Irrigation District (China)
1001 using a remote sensing approach. *Int J Remote Sens* 39: 6805-6825. [https://](https://doi.org/10.1080/01431161.2018.1466076)
1002 doi.org/10.1080/01431161.2018.1466076. 2018.
- 1003 Hanson, B., Hopmans, J., Šimůnek, J.: Leaching with Subsurface Drip Irrigation
1004 under Saline, Shallow Groundwater Conditions. *Vadose Zone J.* 7, 810-818.
1005 <http://doi.org/10.2136/vzj2007.00532008>. 2008.
- 1006 Hsiao, T., Heng, L., Steduto, P., Rojas-Lara, B., Raes, D., Fereres, E.: AquaCrop-The
1007 FAO Crop Model to Simulate Yield Response to Water: III. Parameterization and
1008 Testing for Maize. *Agron. J.*, 101(3):448-459. [https:// doi.org/](https://doi.org/10.2134/agronj2008.0218s)
1009 [10.2134/agronj2008.0218s](https://doi.org/10.2134/agronj2008.0218s). 2009.

- 1010 Hu, S., Shi, L., Huang, K., Zha, Y., Hu, X., Ye, H., Yang, Q.: Improvement of
1011 sugarcane crop simulation by SWAP-WOFOST model via data assimilation.
1012 *Field Crop Res.*, 232: 49-61. [https:// doi.org/10.1016/j.fcr.2018.12.009](https://doi.org/10.1016/j.fcr.2018.12.009). 2019.
- 1013 Huang, Q., Xu, X., Lu, L., Ren, D., Ke, J., Xiong,Y., Huo, Z. and Huang, G.: Soil
1014 salinity distribution based on remote sensing and its effect on crop growth in
1015 Hetao Irrigation District. *Transactions of the Chinese Society of Agricultural*
1016 *Engineering*, 34:102-109. 2018.
- 1017 Kendy, E., Gérard-Marchant, P., Walter, M. T., Zhang, Y., Liu, C., and Steenhuis, T.S.:
1018 A soil-water-balance approach to quantify groundwater recharge from irrigated
1019 cropland in the North China Plain. *Hydrol. Process.*, 17:2011-2031. [https://](https://doi.org/10.1002/hyp.1240)
1020 doi.org/10.1002/hyp.1240. 2003.
- 1021 Leube, P. C., : Temporal moments revisited: Why there is no better way for physically
1022 based model reduction in time, *Water Resour Res*, 48(11): W11527. [https://](https://doi.org/10.1029/2012WR011973)
1023 doi.org/10.1029/2012WR011973 2012.
- 1024 Li, J., Pu, L., Han, M., Zhu, M., Zhang, R., Xiang, Y.: Soil salinization research in
1025 China: Advances and prospects, *J Geogr Sci*, 24(5), 943-960. [https:// doi.org/](https://doi.org/10.1007/s11442-014-1130-2)
1026 [10.1007/s11442-014-1130-2](https://doi.org/10.1007/s11442-014-1130-2) .2014
- 1027 Letey, J., Hoffman, G.J., Hopmans, J.W., Grattan, S.R., Suarez, D., Corwin, D.L.,
1028 Oster, J.D., Wu, L., Amrhein, C.: Evaluation of soil salinity leaching requirement
1029 guidelines. *Agric. Water Manag.* 98, 502–506.
1030 <https://doi.org/10.1016/j.agwat.2010.08.009>. 2011.
- 1031 Li, X., Zhao, Y., Xiao, W., Yang, M., Shen, Y., Min, L.: Soil moisture dynamics and
1032 implications for irrigation of farmland with a deep groundwater table. *Agr. Water*
1033 *Manage.*,192:138-148. [https:// doi.org/ 10.1016/j.agwat.2017.07.003](https://doi.org/10.1016/j.agwat.2017.07.003).2017.
- 1034 Liu, J.: A GIS-based tool for modelling large-scale crop-water relations. *Environ*
1035 *Modell Softw.* 24(3): 411-422. [https:// doi.org/ 10.1016/j.envsoft.2008.08.004](https://doi.org/10.1016/j.envsoft.2008.08.004).
1036 2009.
- 1037 Liu, Z., Wang, X., Huo, Z, Steenhuis, T.S.: A unique vadose zone model for shallow
1038 aquifers: the Hetao irrigation district, China. *Hydrol Earth Syst Sc.*
1039 23(7):3097-3115. [https:// doi.org/ 10.5194/hess-23-3097-2019](https://doi.org/10.5194/hess-23-3097-2019). 2019.

- 1040 Luo, Y., and Sophocleous, M.: Seasonal groundwater contribution to crop-water use
 1041 assessed with lysimeter observations and model simulations. *J. Hydrol*,
 1042 389:325-335. [https:// doi.org/10.1016/j.jhydrol.2010.06.011](https://doi.org/10.1016/j.jhydrol.2010.06.011). 2010.
- 1043 Ma, Y., Feng, S., and Song, X.: A root zone model for estimating soil water balance
 1044 and crop yield responses to deficit irrigation in the North China Plain. *Agr. Water*
 1045 *Manage.*, 127:13-24. [https:// doi.org/10.1016/j.agwat.2013.05.011](https://doi.org/10.1016/j.agwat.2013.05.011). 2013.
- 1046 Miao, Q., Rosa, R., Shi, H., Paredes, P., Zhu, L., Dai, J., Goncalves, J., Pereira, L.:
 1047 Modeling water use, transpiration and soil evaporation of spring wheat–maize
 1048 and spring wheat–sunflower relay intercropping using the dual crop coefficient
 1049 approach. *Agr Water Manage*, 165:211-229.
 1050 <https://doi.org/10.1016/j.agwat.2015.10.024>. 2016.
- 1051 Minhas, P., Ramos, T., Ben-Gal., A., Pereira, L.: Coping with salinity in irrigated
 1052 agriculture: Crop evapotranspiration and water management issues. *Agr Water*
 1053 *Manage*, 227, 105832. [https://doi.org/ 10.1016/j.agwat.2019.105832](https://doi.org/10.1016/j.agwat.2019.105832). 2020.
- 1054 Moriasi, D. N., Arnold, J. G., Van Liew, M. W., Bingner, R. L., Harmel, R. D., Veith, T.
 1055 L.: Model evaluation guidelines for systematic quantification of accuracy in
 1056 watershed simulations. *T ASABE*, 50(3): 885-900. 2007.
- 1057 Nash, J.E., and Sutcliffe, J.V.: River flow forecasting through conceptual models part I
 1058 – a discussion of principles. *J Hydrol*. 10:282-290. 1970.
- 1059 Novark, V.: Estimation of Soil-water Extraction Patterns by Roots, *Agr Water Manage*,
 1060 12(4), 271-278. [https:// doi.org/10.1016/0378-3774\(87\)90002-3](https://doi.org/10.1016/0378-3774(87)90002-3). 1987
- 1061 Phogat, V., Mallants, D., Cox, J., Šimůnek, J., Oliver, D., Awad, J.: Management of
 1062 soil salinity associated with irrigation of protected crops. *Agr. Water Mange.*,
 1063 227:105845. <https://doi.org/10.1016/j.agwat.2019.105845>. 2020.
- 1064 Raes, D., Steduto, P., Hsiao, T., Fereres.: AquaCrop-The FAO Crop Model to
 1065 Simulate Yield Response to Water: II. Main Algorithms and Software Description,
 1066 *Agron. J*, 101(3), 438. [https:// doi.org/10.2134/agronj2008.0140s](https://doi.org/10.2134/agronj2008.0140s). 2009.
- 1067 Regis, R., and Shoemaker, C.: Constrained Global Optimization of Expensive Black
 1068 Box Functions Using Radial Basis Functions, *J Global Optim*, 31(1), 153-171.
 1069 [https:// doi.org/10.1007/s10898-004-0570-0](https://doi.org/10.1007/s10898-004-0570-0). 2005.
- 1070 Ren, D., Xu, X., Hao, Y., and Huang, G.: Modeling and assessing field irrigation water
 1071 use in a canal system of Hetao, upper Yellow River basin: Application to maize,

- 1072 sunflower and watermelon. *J. Hydrol*, 532:122-139. <https://doi.org/10.1016/j.jhydrol.2015.11.040>. 2016.
- 1073
- 1074 Ren, D., Xu, X., Romos, T., Huang, Q., Huo, Z., Huang, G.: Modeling and assessing
1075 the function and sustainability of natural patches in salt-affected
1076 agro-ecosystems: Application to tamarisk (*Tamarix chinensis* Lour.) in Hetao,
1077 upper Yellow River basin. *J. Hydrology*.
1078 532:490-504. <https://doi.org/10.1016/j.jhydrol.2017.04.054>. 2017.
- 1079 Rengasamy, P.: World salinization with emphasis on Australia, *J Exp. Bot.*, 57(5),
1080 1017-1023. <https://doi.org/10.1093/jxb/erj108> .2006
- 1081 Rhoades, J., Manteghi, N., Shouse, P., Alves, W.: Soil Electrical Conductivity and
1082 Soil Salinity: New Formulations and Calibrations, *Soil Sci. Soc. Am. J.*, 53(2):
1083 433-439. <https://doi.org/10.2136/sssaj1989.03615995005300020020x>. 1989.
- 1084 Ritter, A., and Muñoz-Carpena, R.: Performance evaluation of hydrological models:
1085 Statistical significance for reducing subjectivity in goodness-of-fit assessments. *J*
1086 *Hydrol.*, 480:33-45. 2013. <https://doi.org/10.1016/j.jhydrol.2012.12.004>. 2013.
- 1087 Rosa, R.D., Paredes, P., Rodrigues, G.C., Alves, I, Fernando, R.M., Pereira, L.S.,
1088 Allen, R.G.: Implementing the dual crop coefficient approach in interactive
1089 software. 1. Background and computational strategy. *Agr. Water Manage.*, 103:
1090 8-24. <https://doi.org/10.1016/j.agwat.2011.10.013>. 2012.
- 1091 Sau, F., Boote, K., Bostick, W., Jones, J., Minguéz, M.: Testing and improving
1092 evapotranspiration and soil water balance of the DSSAT crop models. *Agron. J.*,
1093 96: 1243-1257. <https://doi.org/10.2134/agronj2004.1243>. 2004.
- 1094 Shelia, V., Simunek, J., Boote, K., Hoogenboom, G.: Coupling DSSAT and
1095 HYDRUS-1D for simulations of soil water dynamics in the soil-plant-atmosphere
1096 system. *J Hydrol Hydromech.*, 66(2): 232-245. <https://doi.org/10.1515/johh-2017-0055>. 2018.
- 1097
- 1098 Šimunek, J., Šejna, M. and van Genuchten, M.T.: The HYDRUS-1D software
1099 package for simulating the one-dimensional movement of water, heat, and
1100 multiple solutes in variably-saturated media. Version 2.0. IGWMC-TPS-70. Int.
1101 Groundwater Modeling Ctr., Colorado School of Mines, Golden. 1998.

- 1102 Steduto, P., Hsiao, T., Raes, D., Fereres, E.: AquaCrop-The FAO Crop Model to
1103 Simulate Yield Response to Water: I. Concepts and Underlying Principles. *Agron*
1104 *J.*, 101(3):426-437. [https:// doi.org/10.2134/agronj2008.0139s](https://doi.org/10.2134/agronj2008.0139s). 2009.
- 1105 Steenhuis, T., Richard, T., Parlange, M., Aburime, S., Geohring, L., PARlange, J.:
1106 Preferential Flow Influences on Drainage of Shallow Sloping Soils. *Agr Water*
1107 *Manage.*, 14(1-4):137-151. [https:// doi.org/ 10.1016/0378-3774\(88\)90069-8](https://doi.org/10.1016/0378-3774(88)90069-8).
1108 1988.
- 1109 Uehara, G.: Technology-transfer in the tropics. *Outlook Agr.*, 18(1): 38-42. [https://](https://doi.org/10.1177/003072708901800107)
1110 [doi.org/ 10.1177/003072708901800107](https://doi.org/10.1177/003072708901800107). 1989.
- 1111 Van Diepen, C., Wolf, J., van Keulen, H., Rappoldt, C.: WOFOST A STIMULATION
1112 MODEL OF CROP PRODUCTION. *Soil Use and Management*, 5(1): 16-24.
1113 1989.
- 1114 Wallender, W. , Tanji, K. : Agricultural salinity assessment and management.
1115 Agricultural salinity assessment and management. Ed.2. American Society of
1116 Civil Engineers (ASCE), Reston, USA. University of California-Davis, USA.:
1117 xxx+1094pp. 2011.
- 1118 Wang, X., Huang, G., Yang, J., Huang, Q., Liu, H., Yu, L.: An assessment of irrigation
1119 practices: Sprinkler irrigation of winter wheat in the North China Plain. *Agr Water*
1120 *Manage.*, 159: 197-208. [https:// doi.org/ 10.1016/j.agwat.2015.06.011](https://doi.org/10.1016/j.agwat.2015.06.011). 2015.
- 1121 Wang, J., Huang, G., Zhan, H., Mohanty, B., Zheng, J., Huang, Q., Xu, X.: Evaluation
1122 of soil water dynamics and crop yield under furrow irrigation witha
1123 two-dimensional flow and crop growth coupled model. *Agr Water Manage.*, 141:
1124 10-22. [https:// doi.org /10.1016/j.agwat.2014.04.007](https://doi.org/10.1016/j.agwat.2014.04.007). 2014.
- 1125 Wu, X., Zheng, Y., Wu, B., Tian, Y., Han, F., Zheng, C.: Optimizing conjunctive use of
1126 surface water and groundwater for irrigation to address human-nature water
1127 conflicts: A surrogate modeling approach. *Agr Water Manage*, 163(1): 380-392.
1128 [https:// doi.org/10.1016/j.agwat.2015.08.022](https://doi.org/10.1016/j.agwat.2015.08.022). 2016.
- 1129 Williams, J., Jones, C., Kiniry, J., and Spanel, D.: The EPIC Crop Growth Model. *T.*
1130 *ASAE*, 32:479-511. 1989.
- 1131 Willcox, K., and Peraire J.: Balanced Model Reduction via the Proper Orthogonal
1132 Decomposition, *AIAA J*, 40(11), 2323-2330. [https:// doi.org/10.2514/2.1570](https://doi.org/10.2514/2.1570).
1133 2002.

- 1134 Xu, X., Sun, C., Qu, Z., Huang, Q., Ramos, T.B., and Huang, G.: Groundwater
1135 Recharge and Capillary Rise in Irrigated Areas of the Upper Yellow River Basin
1136 Assessed by an Agro-Hydrological Model. *Irrig. Drain.*, 64:587-599. <https://doi.org/10.1002/ird.1928>. 2015.
1137
- 1138 Xu, X., Sun, C., Huang, G., Mohanty, B.: Global sensitivity analysis and calibration of
1139 parameters for a physically-based agro-hydrological model. *Environ Modell
1140 Softw.*, 83: 88-102. <https://doi.org/10.1016/j.envsoft.2016.05.013>. 2016.
- 1141 Xu, X., Huang, G., Sun, C., Pereira, L., Ramos, T., Huang, Q., Hao, Y.: Assessing the
1142 effects of water table depth on water use, soil salinity and wheat yield: Searching
1143 for a target depth for irrigated areas in the upper Yellow River basin. *Agr Water
1144 Manage*, 125: 46-60. <https://doi.org/10.1016/j.agwat.2013.04.004>. 2013.
- 1145 Xu, X., Huang, G., Qu, Z., and Pereira, L.S.: Assessing the groundwater dynamics
1146 and impacts of water saving in the Hetao Irrigation District, Yellow River basin.
1147 *Agr Water Manage.*, 98:301-313. <https://doi.org/10.1016/j.agwat.2010.08.025>.
1148 2010.
- 1149 Xue, J., Huo, Z., Wang, F., Kang, S., and Huang, G.: Untangling the effects of shallow
1150 groundwater and deficit irrigation on irrigation water productivity in arid region:
1151 New conceptual model. *Sci. Total Environ.*, 619-620:1170-1182. <https://doi.org/10.1016/j.scitotenv.2017.11.145> 2018.
1152
- 1153 Yang, X., Chen, Y., Pacenka, S., Gao, W., Ma, L., Wang, G., Yan, P., Sui, P., and
1154 Steenhuis, T. S.: Effect of diversified crop rotations on groundwater levels and
1155 crop water productivity in the North China Plain, *J. Hydrol.*, 522, 428–438,
1156 <https://doi.org/10.1016/j.jhydrol.2015.01.010>, 2015a.
- 1157 Yang, X., Chen, Y., Pacenka, S., Gao, W., Zhang, M., Sui, P., and Steenhuis, T. S.:
1158 Recharge and groundwater use in the North China Plain for six irrigated crops for
1159 an eleven year period, *Plos One*, 10, e0115269, <http://doi.org/10.1371/journal.pone.0115269>, 2015b.
1160
- 1161 Yeh, P.J., and Famiglietti, J.S.: Regional groundwater evapotranspiration in Illinois. *J.
1162 Hydrometeorol.*, 10:464-478. <https://doi.org/10.1175/2008JHM1018.1>. 2009.
- 1163 Zhang, B., Kang, S., Zhang, L., Du, T., Li, S., Yang, X.: Estimation of seasonal crop
1164 water consumption in a vineyard using Bowen ratio-energy balance method.
1165 *Hydrol. Process*, 21(6): 3635-3641. <https://doi.org/10.1002/hyp.6568>.

1166 Zhang, F., Zhou, G., Wang, Y., Yang, F., Nilsson, C.: Evapotranspiration and crop
1167 coefficient for a temperate desert steppe ecosystem using eddy covariance in
1168 Inner Mongolia, China. *Hydrol. Process*, 26(3): 379-386. [https:// doi.org/
1169 10.1002/hyp.8136](https://doi.org/10.1002/hyp.8136).